

Infrared Spectral Energy Distribution of Galaxies in the AKARI All Sky Survey: Correlations with Galaxy Properties, and Their Physical Origin

Tomonori TOTANI¹, Tsutomu T. TAKEUCHI^{2,3}, Masahiro NAGASHIMA⁴, Masakazu A.R. KOBAYASHI⁵,
and Ryu MAKIYA¹

¹*Department of Astronomy, School of Science, Kyoto University, Sakyo-ku, Kyoto 606-8502*

²*Institute for Advanced Research, Nagoya University, Furo-cho, Chikusa-ku, Nagoya 464-8601*

³*Department of Particle and Astrophysical Science, Nagoya University, Furo-cho, Chikusa-ku, Nagoya 464-8602*

⁴*Faculty of Education, Nagasaki University, Nagasaki, Nagasaki 852-8521*

⁵*Optical and Infrared Astronomy Division, National Astronomical Observatory, Mitaka, Tokyo 181-8588*

(Received 2011 March 28; accepted 2011 June 18)

Abstract

We have studied the properties of more than 1600 low-redshift galaxies by utilizing high-quality infrared flux measurements of the AKARI All-Sky Survey and physical quantities based on optical and 21-cm observations. Our goal is to understand the physics determining the infrared spectral energy distribution (SED). The ratio of the total infrared luminosity L_{TIR} , to the star-formation rate (SFR) is tightly correlated by a power-law to specific SFR (SSFR), and L_{TIR} is a good SFR indicator only for galaxies with the largest SSFR. We discovered a tight linear correlation for normal galaxies between the radiation field strength of dust heating, estimated by infrared SED fits (U_h), and that of galactic-scale infrared emission ($U_{\text{TIR}} \propto L_{\text{TIR}}/R^2$), where R is the optical size of a galaxy. The dispersion of U_h along this relation is 0.3 dex, corresponding to 13% dispersion in the dust temperature. This scaling and the U_h/U_{TIR} ratio can be explained physically by a thin layer of heating sources embedded in a thicker, optically-thick dust screen. The data also indicate that the heated fraction of the total dust mass is anti-correlated to the dust column density, supporting this interpretation. In the large U_{TIR} limit, the data of circumnuclear starbursts indicate the existence of an upper limit on U_h , corresponding to the maximum SFR per gas mass of $\sim 10 \text{ Gyr}^{-1}$. We find that the number of galaxies sharply drops when they become optically thin against dust-heating radiation, suggesting that a feedback process to galaxy formation (likely by the photoelectric heating) is working when dust-heating radiation is not self-shielded on a galactic scale. Implications are discussed for the M_{HI} -size relation, the Kennicutt-Schmidt relation, and galaxy formation in the cosmological context.

Key words: galaxies: formation—galaxies: ISM—galaxies: statistics—infrared: galaxies—ISM: dust, extinction

1. Introduction

Dust grains in interstellar medium (ISM) absorb ultraviolet and optical photons emitted from stars, and the energy is re-emitted from dust grains in infrared and submillimeter wavelengths. The spectral energy distribution (SED) of this dust emission has a broad peak of the modified blackbody in far-infrared bands from large grains in thermal equilibrium with temperatures of $T_d \sim 10\text{--}50$ K. The SED in near- to mid-infrared bands is, on the other hand, characterized by emissions from small grains and polycyclic aromatic hydrocarbons (PAHs) that have a wide distribution of temperature because of stochastic single-photon heating (Desert et al. 1990; see Draine 2003 for a review). Physical dust models about compositions and size distribution have been developed to calculate SEDs of dust emission for a given heating radiation field strength, U , and one can predict the global SED integrated over a galaxy by summing up the emission from dust with various values of U . Such models have been applied to fit observed SEDs of nearby galaxies to derive

physical quantities (e.g., Dale et al. 2001; Dale & Helou 2002; Draine et al. 2007; da Cunha et al. 2008, 2010; Muñoz-Mateos et al. 2009; Małek et al. 2010).

The intensity of the cosmic infrared background radiation indicates that about half of the energy originally radiated from stars is eventually re-emitted from dust grains (Hauser & Dwek 2001). Heavily obscured star formation activity is difficult to detect by observations in ultraviolet/optical observations, and infrared/submillimeter observations should crucially be important to get the full picture of the formation and evolution of galaxies. In the last decade, our observational knowledge about the hidden side of galaxy evolution has significantly improved thanks to the advanced infrared/submillimeter facilities such as JCMT/SCUBA, Spitzer, AKARI, and Herschel. Moreover, the Atacama Large Millimeter/submillimeter Array (ALMA) will revolutionize our understanding of galaxy evolution in the near future. In order to extract useful information from these data, we need good theoretical understanding and models of galactic dust emission to be compared.

However, it is not straightforward to predict global (i.e., galactic-scale) SEDs of dust emission for a theoretical model galaxy, in contrast to direct stellar emission that can be calculated by the method of stellar population synthesis. This is because the physics determining the global SED of dust emission and its relations to other physical properties have remained highly elusive (see Walcher et al. 2011 for a review). An approach often taken in the literature (e.g., Guiderdoni et al. 1998; Takeuchi et al. 2001; Chary & Elbaz 2001; Lagache, Dole, & Puget 2003; Valiante et al. 2009) is to relate the SED parameter (e.g., the dust temperature T_d) to the total infrared luminosity, L_{TIR} (defined as the bolometric luminosity of dust emission), based on the observed correlation between the two (higher T_d for larger L_{TIR} ; Soifer et al. 1987a; Soifer & Neugebauer 1991; Chapin et al. 2009). However, there is a large scatter along the mean $L_{\text{TIR}}-T_d$ relation (see, e.g., Hwang et al. 2010 for recent data), and it is physically unreasonable to relate an extensive quantity L_{TIR} that scales with the system size to an intensive quantity T_d that does not (Totani & Takeuchi 2002). Extension of this relation including another parameter has also been discussed, e.g., galaxy size (Devereux 1987; Phillips & Disney 1988; Lehnert & Heckman 1996; Chanical et al. 2007; Rujopakarn et al. 2011a,b), but a consistent physical picture has not yet been established.

To make a completely theoretical prediction, one must solve transfer of dust heating radiation taking into account complicated geometry in a galaxy. Infrared SED models by such *ab initio* approaches have also been developed (Silva et al. 1998; Takagi et al. 2003a, b; Dopita et al. 2005), and applied to predict infrared SEDs in galaxy evolution models (Granato et al. 2000; Baugh et al. 2005; Fontanot et al. 2007). However, it is difficult to calculate detailed geometry within galaxies in models on the cosmological scale, and one must add many uncertain and adjustable model parameters, making it difficult to extract useful information from comparison with observed data.

Therefore it is still important to investigate the relation between infrared SEDs and various physical properties to find any correlation that would be useful to better understand the galactic-scale radiation from dust grains. The recently released catalogs of the AKARI All Sky Survey (Ishihara et al. 2010; Yamamura et al. 2010) for sources detected by the AKARI satellite (Murakami et al. 2007) provide us with a new opportunity to investigate nearby galaxies for this purpose. The Infrared Camera (IRC, Onaka et al. 2007) and the Far-Infrared Surveyor (FIS, Kawada et al. 2007) on board the satellite have detected more than 800000 and 400000 sources in 9–18 and 65–160 μm bands, respectively. For recent studies on galaxies using samples based on these catalogs, see Takeuchi et al. (2010), Buat et al. (2011), Goto et al. (2011a, b), and Yuan et al. (2011).

Especially, the four FIS bands at 65–160 μm should be very useful to accurately measure the modified blackbody peak of the dust emission SEDs, as they cover the wavelength range around the peak by a larger number of pho-

tometric bands with better flux sensitivity and angular resolution than those of the previous infrared all-sky survey by the Infrared Astronomical Satellite (IRAS, Soifer et al. 1987b). In this paper we perform SED fittings of physical dust models to the AKARI data of more than 1600 low-redshift galaxies, and compare the SED parameters with other physical properties of galaxies obtained by optical and 21-cm observations. The goal of this paper is to find the key physical quantities and laws to determine the global SEDs of dust emission (especially around the thermal peak), and give physical interpretations to them.

In §2 we describe the construction of the galaxy samples used in this work. The physical dust models and SED fittings to the AKARI data are described in §3. We then present theoretical background and considerations in §4, which will be used to interpret the results obtained in this work. The main results are presented in §5, followed by discussions in §6 and summary in §7. We adopt the standard cosmological parameters of $H_0 = 70 \text{ km s}^{-1} \text{ Mpc}^{-1}$, $\Omega_M = 0.3$, and $\Omega_\Lambda = 0.7$, though the choice of the cosmological parameters hardly affects our results based on galaxies at low redshifts.

2. The Samples

2.1. The AKARI All-Sky Survey

We use the AKARI/IRC All-Sky Survey Point Source Catalog (PSC, ver. 1.0) and the AKARI/FIS All-Sky Survey Bright Source Catalog (BSC, ver. 1.0), which were released in March 2010 including 870973 and 427071 sources, respectively. The IRC provides fluxes in two photometric bands, *S9W* and *L18W*, whose central wavelengths (λ_c) are 9 and 18 μm , respectively. The FIS provides fluxes in the four photometric bands of *N60*, *WIDE-S*, *WIDE-L*, and *N160*, whose central wavelengths are 65, 90, 140, and 160 μm , respectively. The sensitivity limits corresponding to 50% detection completeness are shown in Table 1, and the relative spectral response functions (RSRFs) for the six bands are shown in Fig. 1. See the release notes of these catalogs available on the AKARI web site for more details.

Since the SED fitting is the central issue of this work, treatment of flux errors is important. In this work we consider only statistical flux errors associated with each flux measurements, and systematic errors that are common for all sources (e.g., flux calibration errors) are not taken into account. Systematic errors would result in systematic bias in SED fit parameters (e.g., a systematic shift of dust temperature), but it does not seriously affect the study of correlation or trend between the fit parameters and other galaxy properties. Statistical errors can be divided into two parts: one is the error that does not depend on source fluxes (denoted as ΔF_{const}), and the other is the error that is proportional to flux ($\Delta F = \epsilon F$). The total flux error is assigned for a flux measurement in a band as:

$$\Delta F_{\text{tot}} = [(\Delta F_{\text{const}})^2 + (\epsilon F)^2]^{\frac{1}{2}}. \quad (1)$$

For faint sources ΔF_{const} is dominant while ϵF is dominant for bright sources. The 1σ values of ΔF_{const} and ϵ

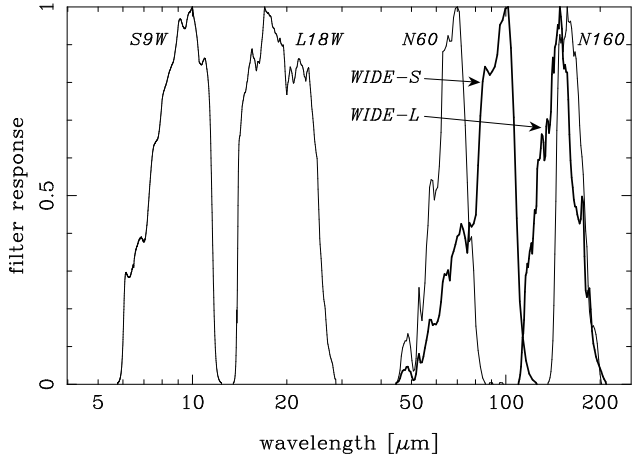


Fig. 1. The relative spectral response function (RSRF) against energy flux for the two AKARI/IRC bands (*S9W* and *L18W*) and the four AKARI/FIS bands (*N60*, *WIDE-S*, *WIDE-L*, and *N160*). The RSRFs are normalized by their maximum values.

for each band are estimated from the signal-to-noise distributions presented in the release notes of the AKARI catalogs, and they are summarized in Table 1.

2.2. Cross-Matches with Optical and 21cm Data

We construct the following three samples by cross-matching the AKARI catalogs with the existing catalogs of nearby galaxies selected in other wavelengths. The first sample is the cross-match with the galaxies detected by the Sloan Digital Sky Survey (SDSS), and the second with the HI Parkes All-Sky Survey (HIPASS) selected by 21-cm flux. We regard these as the two main samples in this paper, and we can check the dependence on the sample selection by these two. In addition, we construct the third sample to extend the dynamic range of surface density of star formation rate (SFR), which is the cross-match with the Kennicutt (1998, hereafter K98) sample of nearby circumnuclear starburst (SB) galaxies. The summary of constructing these samples, showing galaxy numbers at various stages of selections, is presented in Table 2.

2.2.1. The AKARI-SDSS Sample

We first extracted a sample of 1 145 617 SDSS galaxies having measured redshifts from the DR7 NYU Value-Added Galaxy Catalog (NYU-VAGC, Blanton et al. 2005). The information of apparent Petrosian magnitudes in the five *ugriz* bands, (Galactic) extinction- and *K*-corrected absolute magnitudes, and *r*-band Petrosian 90% angular radii that include 90% of Petrosian flux (θ_{P90}) will be used in the analyses of this work. We take θ_{P90} from several size estimations available for SDSS galaxies, since this size is not sensitive to central concentration (Nair et al. 2010). The angular sizes are converted into physical radii as $R_{P90} = d_A(z) \theta_{P90}$, where d_A is the standard angular diameter distance to redshift z .

These galaxies were cross-matched separately with the AKARI/IRC and AKARI/FIS catalogs, with the matching radius of 5 and 20 arcsec, respectively. The mean

positional errors of sources in these catalogs are 0.8 and 6 arcsec, and essentially all objects should fall within the matching radii. [See also Table 1 for the instrumental point spread functions (PSF) in each band.] To avoid contamination of random associations, we removed any duplications, i.e., AKARI galaxies having more than two SDSS counterparts, and vice versa. We then obtained 390 and 6500 matches of SDSS galaxies with the IRC and FIS catalogs, respectively. The expected random associations are 25.1 and 143.7 for SDSS-IRC and SDSS-FIS, if the sources are uniformly distributed on the sky. These numbers are sufficiently small for studying the overall and statistical trends of galactic properties. Because the number of cross-matches with the IRC catalog is small, we construct the AKARI-SDSS sample based on the correlation between the SDSS and FIS catalogs, without requiring detection by IRC.

To keep good quality of the data, we further selected galaxies satisfying the following conditions: $z \geq 0.005$, $r \leq 16.0$ mag, $\theta_{P90} \geq 6.0''$, and the AKARI/FIS flux quality flag¹ $FQUAL \geq 3$ in at least two FIS bands. The redshift condition is to remove too close objects whose redshift-based distance is rather uncertain by the peculiar velocity effect. The magnitude and size conditions are to keep good quality of size estimates and to make the seeing effect negligible. The condition for $FQUAL$ is for reliable SED fittings. Then 878 galaxies qualified as the final AKARI-SDSS sample. The numbers of galaxies with $FQUAL \geq 1$ or 3 in each FIS band are shown in Table 3. This table shows that the 90- and 140- μ m bands are more sensitive than the other two bands and most galaxies are detected in these bands with $FQUAL \geq 3$.

To these galaxies we added physical quantities derived from SDSS spectra by the MPA/JHU group when they are available, by cross-matching the spectroscopic ID [plate number, Mean Julian Date (MJD), and fiber number]. Stellar mass (M_* , Kauffmann et al. 2003; Salim et al. 2007), SFR (ψ , Brinchmann et al. 2004), and gas-phase metallicity (Tremonti et al. 2004) of the DR7 version are available for 550, 567, and 246 galaxies, respectively, in the total sample of the 878 galaxies. The metallicity is given in $A_O \equiv 12 + \log_{10}(O/H)$ in the original data, but in this work we use metallicity Z converted² from A_O using $A_{O\odot} = 8.69$ and $Z_{\odot} = 0.02$. We also added the *V* band optical depth τ_V of stellar light attenuation by dust in galaxies, estimated by Tojeiro et al. (2009) using the VESPA algorithm (the one-parameter dust model in the RunID=1 catalog), to 534 galaxies.

We also added information of neutral hydrogen (HI) mass from 21-cm observations in the literature. SDSS galaxies were cross-matched with the optical counterpart

¹ See the release note of the AKARI/FIS catalog for the definition of $FQUAL$. It is recommended not to use the flux data when $FQUAL \leq 2$ for a reliable scientific analysis.

² There are systematic uncertainties in estimates of A_O , Z , and their solar values (Grevesse et al. 2010; Moustakas et al. 2010). We will mostly discuss correlations between metallicity and other physical parameters, and absolute uncertainty does not significantly affect our conclusions.

Table 1. Summary of the AKARI All-Sky Survey Parameters

instrument band name	IRC		FIS			
	<i>S9W</i>	<i>L18W</i>	<i>N60</i>	<i>WIDE-S</i>	<i>WIDE-L</i>	<i>N160</i>
central wavelength λ_c [μm]	9	18	65	90	140	160
flux sensitivity* [Jy]	0.09	0.17	2.6	0.39	2.9	5.9
ΔF_{const} [Jy]	0.02	0.04	0.48	0.11	0.28	1.26
ϵ [%]	5.6	6.7	10	10	10	10
PSF [arcsec FWHM]	5.6	5.6	37	39	58	61

*The flux where the source detection completeness is 50%.

Table 2. The Summary of Sample Construction

	AKARI-SDSS	AKARI-HIPASS	AKARI-SB
original catalog	1145617	4315	36
match with AKARI/FIS	6500	1527	34
FIS flux quality flag	1138	840	33
distance cut*	996	711	32
magnitude & size cut [†]	878	–	31
$L_{\text{TIR,K98}}/L_{\text{TIR}} \geq 0.5$	–	–	24
final sample	878	711	24
stellar mass [‡]	550	0	0
star formation rate [‡]	567	0	0
metallicity [‡]	246	0	0
τ_V	534	0	0
H I gas mass	257	711	0
H ₂ gas mass	0	0	24

Notes. — The upper six rows show the numbers of galaxies after applying certain selection criteria in the process of constructing the samples. The lower six rows show the numbers of galaxies for which a certain physical quantity is available.

*The condition of $z \geq 0.005$ for AKARI-SDSS and AKARI-HIPASS, while $z \geq 0.005$ or availability of redshift-independent distance is required for AKARI-SB.

[†]The condition of $r \leq 16.0$ mag and $\theta_{P90} \geq 6''$ is adopted for AKARI-SDSS, while a galaxy without diameter size in the K98 sample is excluded from AKARI-SB.

[‡]Physical quantities derived from SDSS optical spectra.

positions of 21-cm-detected galaxies in the data sets of Springob et al. (2005), the ALFALFA survey (Giovanelli et al. 2007; Kent et al. 2008; Stierwalt et al. 2009), the Equatorial Survey (Garcia-Appadoo et al. 2009; West et al. 2010), and the GALEX Arecibo SDSS Survey (Catinella et al. 2010). We found 257 H I flux data available for the AKARI-SDSS sample, and calculated the H I mass from the standard formula³:

$$M_{\text{HI}} = \frac{2.36 \times 10^5}{(1+z)^2} \left(\frac{d_L(z)}{\text{Mpc}} \right)^2 \left(\frac{S_{\text{int}}}{\text{Jy km/s}} \right) M_{\odot}, \quad (2)$$

where $S_{\text{int}} \equiv \int S_{\nu} dV$ is the velocity-integrated flux density and d_L is the standard luminosity distance. For comparison, we also constructed the SDSS-H I sample, for all SDSS galaxies with available H I data without requiring the detection by AKARI. Other selection criteria were kept same as the AKARI-SDSS sample. The SDSS-H I sample consists of 2413 galaxies.

³ The factor of $(1+z)^{-2}$ arises as follows. The H I mass can be written as $M_{\text{HI}} \propto d_L^2 \int S_{\nu} d\nu = d_L^2 \int (d\nu/dV) S_{\nu} dV$, where ν is the observed frequency. In H I observations, the velocity V is defined as $\nu = \nu_{21}/(1+V/c)$ where $\nu_{21} \equiv 1.42$ GHz, and hence $d\nu/dV \propto (1+V/c)^{-2} \sim (1+z)^{-2}$ when the intrinsic velocity dispersion ΔV in a galaxy is much smaller than cz .

Table 3. The Number of Galaxies against AKARI/FIS Flux Quality Flags

sample	condition	FIS bands [μm]			
		65	90	140	160
AKARI-SDSS	$FQUAL \geq 1$	878	878	878	878
	$FQUAL \geq 3$	178	876	851	136
AKARI-HIPASS	$FQUAL \geq 1$	710	711	711	710
	$FQUAL \geq 3$	173	704	700	239
AKARI-SB	$FQUAL \geq 1$	24	24	24	24
	$FQUAL \geq 3$	21	22	24	23

2.2.2. The AKARI-HIPASS Sample

Since the gas amount of galaxies is crucial for the dust amount, we also cross-correlated the AKARI galaxies with the HIPASS catalog (HICAT, Meyer et al. 2004), which is a catalog of 4315 galaxies selected by the H I 21-cm line flux covering the entire southern sky. We selected HIPASS galaxies having optical counterparts from the HOPCAT catalog (Doyle et al. 2005), for which the information of 21-cm line flux, 21-cm redshift, optical magnitudes of B_j , R , and I , and the major axis size $\theta_{A,\text{HOP}}$ of R -band images are extracted from the catalog. The distances were calculated from 21-cm redshifts, and then M_{HI} was calculated from eq. (2). Absolute optical magnitudes were also calculated, correcting the Galactic extinction but ignoring

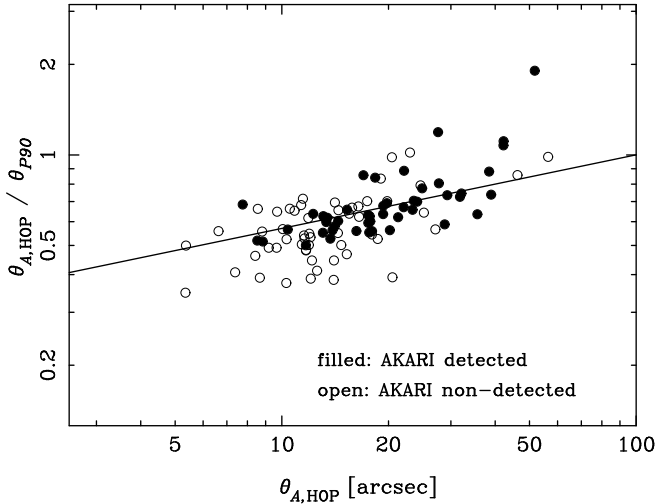


Fig. 2. Correlation between the r -band 90% Petrosian angular radius (θ_{P90}) of SDSS and the R -band major axis size ($\theta_{A,HOP}$) of HOPCAT for galaxies commonly included in the SDSS and HIPASS samples. Filled circles are galaxies detected by AKARI/FIS.

K -correction.

Then the HIPASS galaxies were cross-matched with the AKARI catalogs by the same procedures as those for the AKARI-SDSS sample. We found 161 and 1527 matches with the IRC and FIS catalogs, respectively. Following the AKARI-SDSS sample, we do not require detection by IRC for the AKARI-HIPASS sample. To keep good qualities, we further require the same criteria about redshift ($z \geq 0.005$) and FIS quality flags ($FQUAL \geq 3$ at least in two FIS bands) as the AKARI-SDSS sample, resulting in the final AKARI-HIPASS sample of 711 galaxies.

Because the optical magnitude and size of HOPCAT are from photographic plates, their quality and reliability should carefully be examined. To directly compare the AKARI-SDSS and AKARI-HIPASS samples, we converted the HOPCAT magnitude (R) and size ($\theta_{A,HOP}$) into those in the SDSS catalog (r magnitude and θ_{P90}), and will use these in the following analyses. For this conversion, we first searched for galaxies that are common in SDSS and HOPCAT by optical positions, and found 103 galaxies that satisfy the same criteria as the AKARI-SDSS galaxies about redshift, magnitude, and size. In these galaxies 47 are detected by AKARI/FIS. From comparison between SDSS r and HOPCAT R bands, we apply the following conversion: $R(\text{HOP}) - r(\text{SDSS}) = 0.09$, and the dispersion around this relation is 0.46 mag. Figure 2 shows the comparison between the SDSS size θ_{P90} and the HOPCAT size $\theta_{A,HOP}$, and the ratio $\theta_{A,HOP}/\theta_{P90}$ systematically varies with $\theta_{A,HOP}$. We therefore convert the HOPCAT size into θ_{P90} by the following equation:

$$\log_{10} \left(\frac{\theta_{A,HOP}}{\theta_{P90}} \right) = -0.489 + 0.245 \log_{10} \left(\frac{\theta_{A,HOP}}{\text{arcsec}} \right) \quad (3)$$

which is shown in Fig. 2 by the solid line.

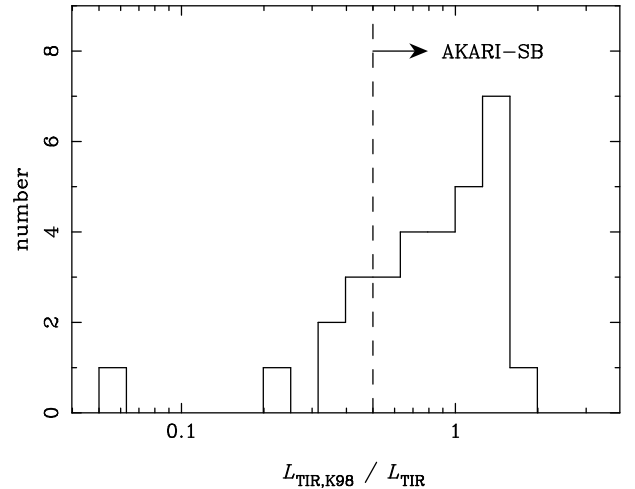


Fig. 3. The histogram of $L_{\text{TIR,K98}}/L_{\text{TIR}}$ for the K98 starburst sample, where $L_{\text{TIR,K98}}$ is the total infrared luminosity from the circumnuclear starburst regions given in Kennicutt (1998) and L_{TIR} is the total infrared luminosity from the whole region of galaxies estimated by SED fittings to the AKARI data in this work. Only galaxies having $L_{\text{TIR,K98}}/L_{\text{TIR}} \geq 0.5$ are used as the AKARI-SB sample.

2.2.3. The AKARI-SB Sample

The AKARI/FIS catalog was cross-matched with the 36 galaxies of the K98 circumnuclear starburst sample by the same procedures as the two samples described above, and we found that 34 galaxies are detected by FIS. To keep the quality of the data, we again adopt the same condition about the FIS flux quality flags. For these galaxies we collected the redshift-independent distance measurements from the NASA Extragalactic Data base (NED), and adopted the mean value when more than one measurements are available for a galaxy. For galaxies that do not have a redshift-independent distance measurement, we calculated the distances from redshifts, but NGC 5194 was removed from the sample because $z < 0.005$. We will use the information of the angular diameter size θ_D , SFR surface density Σ_{SFR} , and H_2 gas mass surface density Σ_{H_2} given in K98. Here, NGC 3256 was removed because θ_D is unavailable.

In K98, SFR and H_2 mass were estimated from L_{TIR} and CO line luminosity, respectively. As argued in K98, L_{TIR} is a good SFR indicator for these starburst galaxies because L_{TIR} is dominated by young stars and dust opacity is large. The SFR- L_{TIR} conversion factor of K98 assumes the Salpeter (1955) initial mass function (IMF), and we divided K98 SFRs by 1.5 to match the SFRs in the AKARI-SDSS sample assuming the Kroupa (2001) IMF (Brinchmann et al. 2004). In this case the SFR (denoted as ψ) is related to L_{TIR} as:

$$\frac{L_{\text{TIR}}}{L_{\odot}} = 8.7 \times 10^9 \left(\frac{\psi}{M_{\odot} \text{ yr}^{-1}} \right). \quad (4)$$

It should be noted that in this work this relation is used only for the AKARI-SB sample; we do not use L_{TIR} as a SFR indicator for the AKARI-SDSS or AKARI-HIPASS

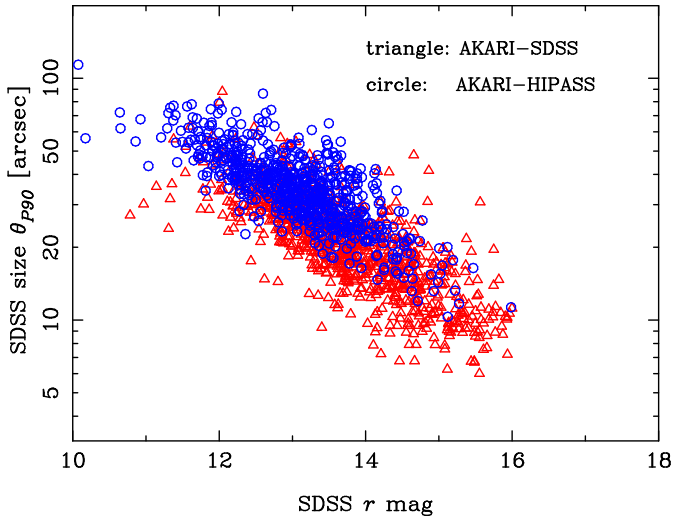


Fig. 6. Comparison between the AKARI-SDSS and AKARI-HIPASS samples in the plot of Petrosian 90% angular radius (θ_{P90}) versus SDSS r magnitude, after the conversion of the HOPCAT R and $\theta_{A,HOP}$ into the SDSS quantities as described in the text.

samples, because a significant fraction of L_{TIR} comes from dust heating by relatively aged stars (see §5.1). SFRs from SDSS spectra will be used for the AKARI-SDSS sample.

The surface densities (Σ_{H2} and Σ_{SFR}) given in K98 are converted into the total quantities (M_{H2} and ψ), e.g., $M_{H2} = \pi R^2 \Sigma_{H2}$, where $R = \theta_D d_A/2$ is the physical radius of circumnuclear starburst regions. Note that the “total” quantities in the AKARI-SB sample are the total within the circumnuclear starburst regions rather than the entire galaxies. Since the AKARI photometries are for the whole region of galaxies, we must examine whether the AKARI fluxes are mostly coming from the circumnuclear regions. For this purpose, we compared the total infrared luminosity from a circumnuclear region, $L_{TIR,K98}$, of the K98 sample (calculated from Σ_{SFR} and θ_D) with L_{TIR} for the entire galaxy newly obtained by our SED fit to the AKARI data (see §3), in Fig. 3. It can be seen that many galaxies have $L_{TIR} \sim L_{TIR,K98}$, indicating that the total infrared luminosities of galaxies are dominated by those from circumnuclear starburst regions. We adopted the condition of $L_{TIR,K98} \geq 0.5 L_{TIR}$ for our sample, to remove galaxies whose infrared luminosity is mostly emitted from outer regions. Then finally we obtained the AKARI-SB sample consisting of 24 galaxies.

2.3. The Basic Properties of the Sample Galaxies

Figure 4 shows redshift versus the AKARI 90- μm flux for the final AKARI-SDSS and AKARI-HIPASS samples. The sensitivity of the 90- μm band is the best among the four FIS bands. Sources are distributed down to the flux sensitivity limit, but the mean flux is considerably brighter than the flux distribution of all FIS-BSC sources reported in the release note, because we have set the condition of $FQUAL \geq 3$ at least in two FIS bands. The mean redshift

of the AKARI-SDSS sample ($z \sim 0.03$) is slightly higher than that of the AKARI-HIPASS sample ($z \sim 0.01$).

Figure 5 shows angular size versus apparent optical magnitude (r for SDSS and R for HIPASS). Compared with the typical SDSS magnitudes, the AKARI-SDSS galaxies are much brighter, indicating that the AKARI sensitivity limit is brighter than SDSS for typical galaxy SEDs. In Fig. 6, we show the size-magnitude plot of the AKARI-HIPASS galaxies when the R magnitude and $\theta_{A,HOP}$ are converted into r and θ_{P90} , in comparison with the AKARI-SDSS galaxies. The distributions of the two samples are similar, indicating that the conversion of magnitude and size is working well.

Figure 7 shows the optical color versus absolute magnitude relation (see also Takeuchi et al. 2010). Our samples cover a wide range of galaxy colors, though the AKARI-SDSS galaxies have a slightly redder mean color than the mean SDSS distribution, indicating that we are sampling dusty galaxies. Red and brightest SDSS galaxies are not detected by AKARI, because they are early-type red-sequence galaxies with no or low star formation activity.

Figure 8 shows the stellar mass (M_*) versus metallicity relation of the AKARI-SDSS sample, which indicates that we are sampling relatively massive and high metallicity galaxies compared with general SDSS galaxies. This is reasonable for our samples limited by the AKARI sensitivity, because massive star-forming galaxies are generally dusty and high metallicity is required for a large amount of dust.

Figure 9 shows V band attenuation τ_V versus specific star formation rate (SSFR) $\psi_s \equiv \psi/M_*$ for the AKARI-SDSS sample (see also Takeuchi et al. 2010). The SDSS galaxies without AKARI detection are bimodally distributed in SSFR reflecting the well known populations of the red sequence and the blue cloud (e.g., Strateva et al. 2001; Bell et al. 2004). The AKARI-detected galaxies are distributed in the high SSFR and high τ_V region, in agreement with the general expectation that recent star formation and a large dust optical depth are necessary for a galaxy to be bright in far-infrared wavelength. However, our sample covers a wide range of SSFR and τ_V , indicating that it includes galaxies having a wide range of star formation history and dust opacity.

Finally Figure 10 shows M_{HI} versus redshift for the AKARI-SDSS and AKARI-HIPASS samples. The HIPASS catalog is limited by HI flux, and this can clearly be seen in the z - M_{HI} relation in the right panel. The effect of HI flux sensitivity limit is also seen for the AKARI-SDSS sample, though it is less clear because of the heterogeneous flux limits of the HI data in the literature. Galaxies detected by AKARI have higher HI mass on average at a fixed redshift than those without AKARI-detection, and hence the AKARI sensitivity limit is also important for these samples.

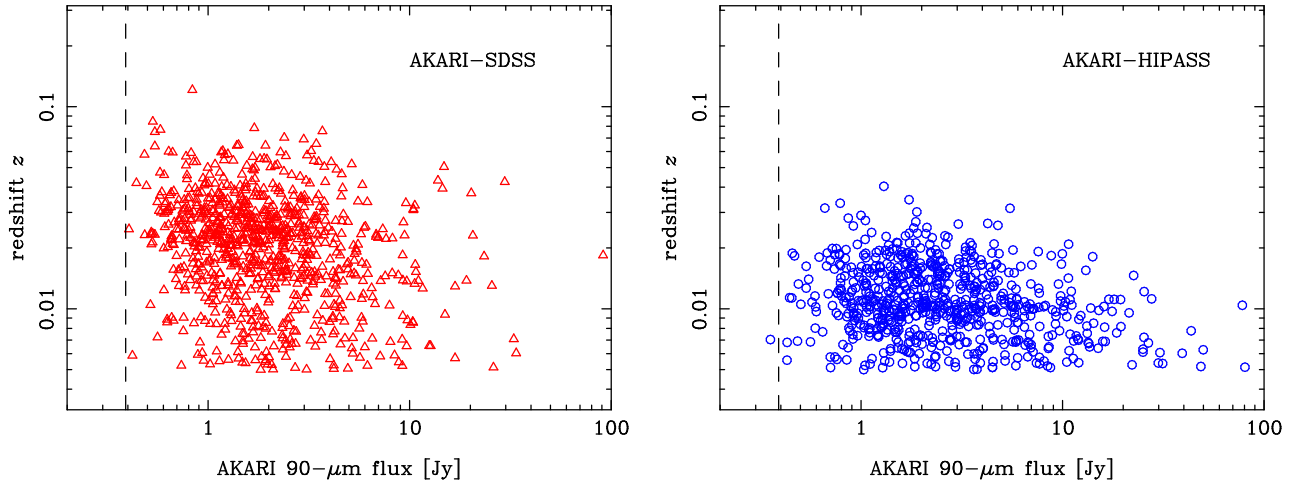


Fig. 4. Redshift versus AKARI 90- μm band flux for the AKARI-SDSS (left) and AKARI-HIPASS (right) samples. The dashed lines indicate the flux sensitivity limit (the flux where the detection completeness is 50%).

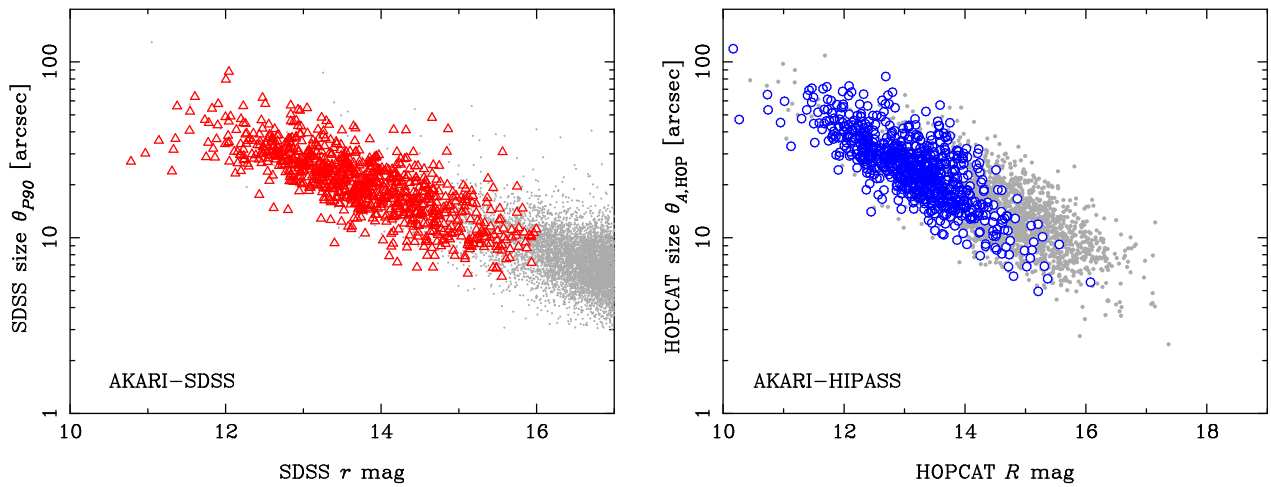


Fig. 5. Angular size versus optical magnitude for the AKARI-SDSS (left) and AKARI-HIPASS (right) samples. The grey dots are galaxies in the original SDSS or HIPASS catalog, without requiring detection by AKARI. The grey dots in the left panel are randomly selected from the whole SDSS catalog because of the large sample size of SDSS.

3. Fitting Physical Dust Models to Infrared SEDs

3.1. The Physical Dust Models

We mainly use the physical dust model of Draine & Li (2007, hereafter DL07) to derive physical quantities about dust emission (see also Weingartner & Draine 2001; Li & Draine 2001). To reduce the number of model parameters, we choose the $j_M = 5$ model of DL07 for the Milky Way (MW) that has the PAH mass fraction of $q_{\text{PAH}} = 3.19\%$, because this PAH fraction is close to the median of nearby galaxies studied by Draine et al. (2007). The normalization of the DL07 model is determined by the hydrogen mass M_{H} , assuming the dust-to-hydrogen mass ratio of $f_{\text{dH}} \equiv M_{\text{d}}/M_{\text{H}} = 0.01$, but f_{dH} likely depends on properties of galaxies, especially metallicity. Therefore in this work we quote the dust mass as the normalization parameter in the SED fitting, rather than the hydrogen mass.

The dust mass inferred from infrared SED fittings is denoted by M_{dIR} , to make a distinction from the total dust mass M_{d} in a galaxy potentially including cold dust that is not heated by radiation and hence not contributing to infrared emission.

The basic parameter of infrared emission in the physical dust model is the heating radiation field strength, U , which is the dimensionless energy density of dust-heating radiation normalized by the local value of the interstellar radiation field (ISRF) around the solar neighbourhood. In reality, the field strength can be different at different locations in a galaxy, and model infrared emission is often calculated considering the dust mass distribution dM_{dIR}/dU as a function of U (Dale et al. 2001; Dale & Helou 2002; DL07). However, the functional form of dM_{dIR}/dU is highly uncertain, making it difficult to interpret the results of infrared SED fittings in a model-independent way.

Here we take a different approach by assuming that in-

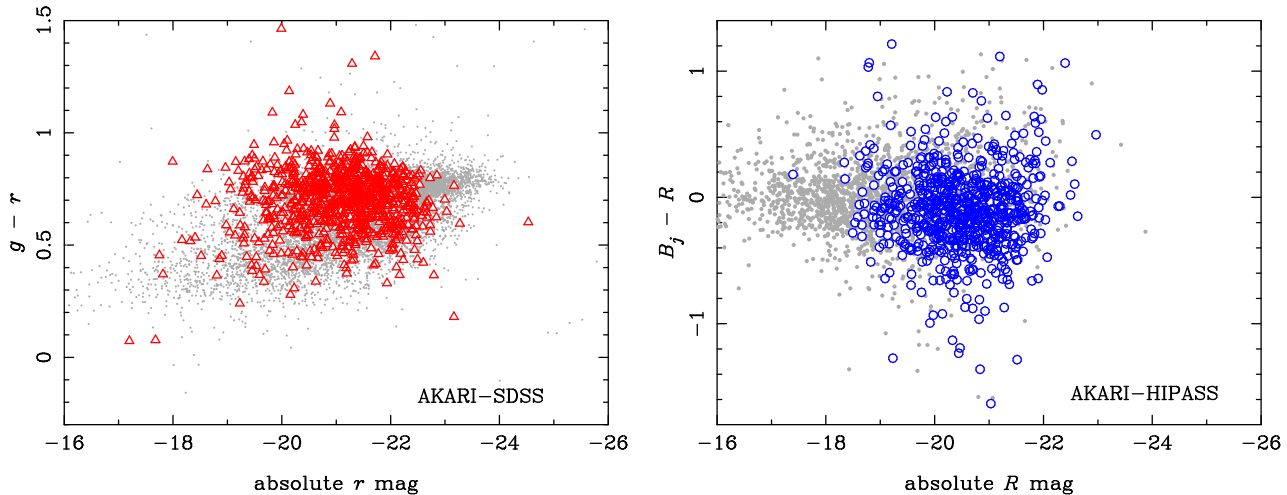


Fig. 7. The same as Fig. 5, but for optical color versus absolute optical magnitude. Colors were calculated from absolute magnitudes, which have been corrected for the Galactic extinction. The K -correction has been done for the SDSS magnitudes but not for the HIPASS magnitudes.

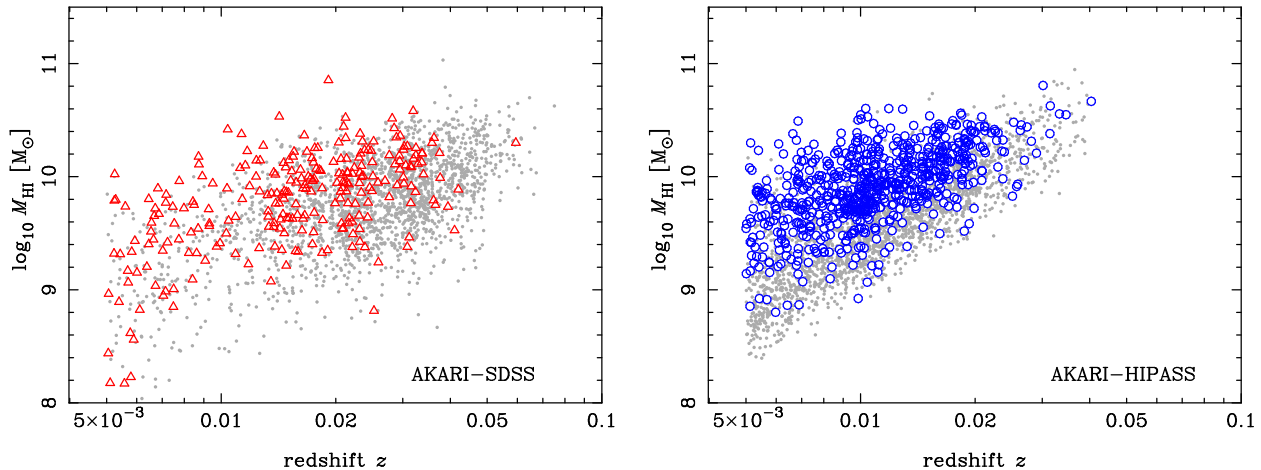


Fig. 10. Neutral hydrogen mass versus redshift for the AKARI-SDSS (left) and AKARI-HIPASS (right) samples. The grey dots are galaxies in the original SDSS or HIPASS catalog, without requiring detection by AKARI.

frared emission from a galaxy can be described by a single characteristic heating radiation strength, U_h . Although it may be difficult to fit observed infrared SEDs in a wide wavelength range from near- to far-infrared by a single value of U , in this work we concentrate on the fitting in a relatively narrow range of wavelength covered by AKARI/FIS (65–160 μm), corresponding to the broad SED peak of modified blackbody. Therefore, U_h in this work should be regarded as the characteristic value for large grains contributing to the thermal emission. An advantage of this approach is that physical discussion based on the radiation field strength becomes easier. The SEDs of the single- U DL07 model for several values of U_h are plotted in Fig. 11.

It would be convenient to compare the SEDs of the physical dust model with the modified blackbody spectra often used in the literature. It is known that SEDs around the thermal peak can be approximated by a mod-

ified blackbody⁴ with the emissivity index of $\beta \sim 1\text{--}2$, i.e., flux density per unit frequency $F_\nu(\nu) \propto Q_{\text{em}}(\nu) B_\nu(\nu, T_d)$, where B_ν is the blackbody spectrum of temperature T_d and $Q_{\text{em}} \propto \nu^\beta$ is the emissivity of dust particles (e.g. Dunne et al. 2000; Kovács et al. 2006). The total infrared luminosity of the modified blackbody scales as $L_{\text{TIR}} \propto T_d^{4+\beta}$, and the νF_ν peak scales as $\nu_{\text{peak}} \propto T_d$. Since $L_{\text{TIR}} \propto U_h$ for a fixed dust mass, we expect $U_h \propto \nu_{\text{peak}}^{4+\beta}$. The relation between U_h and ν_{peak} of the DL07 model implies $\beta = 1.75$, and for this value the modified blackbody with $T_d = 15, 22, 33,$ and 49 K has the same ν_{peak} as the single- U DL07 model of $U_h = 0.1, 1, 10,$ and 100 , respectively. These spectra are also plotted in Fig. 11.

⁴ In the astronomical literature, this is also often referred to as “greybody”, but we avoid this word because strictly it is defined as emission with a constant emissivity less than one against wavelength.

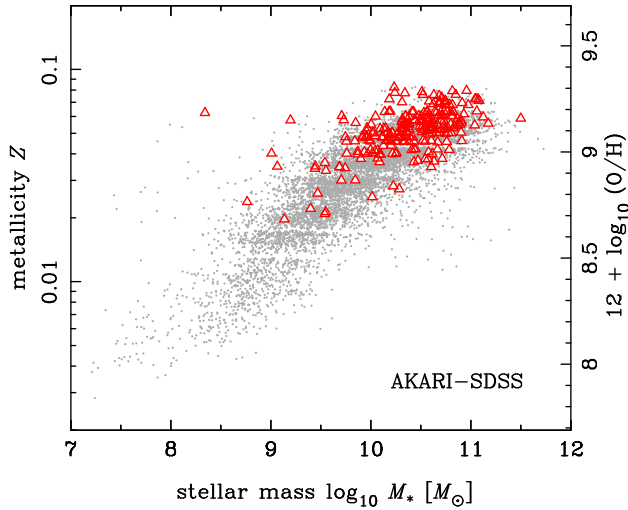


Fig. 8. The stellar mass versus metallicity relation of galaxies in the AKARI-SDSS sample. The grey dots are galaxies without AKARI-detection, randomly selected from the original SDSS catalog.

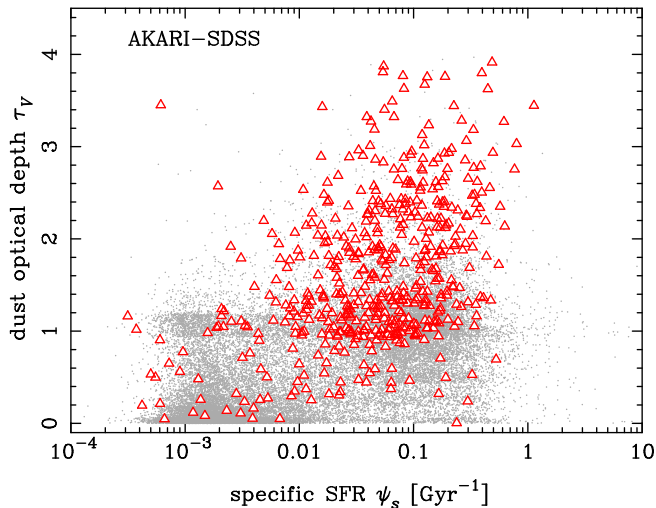


Fig. 9. The same as Fig. 8, but for V-band optical depth of dust in galaxies (τ_V) versus specific star formation rate ($\psi_s \equiv \psi/M_*$).

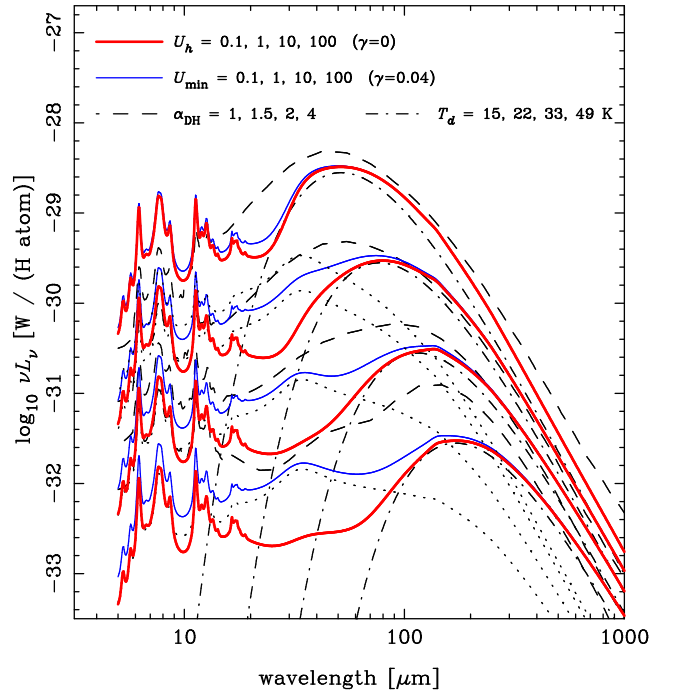


Fig. 11. The infrared SED models of galaxies. The red thick solid curves are the single- U predictions by the physical dust model of DL07, for several values of U_h indicated in the figure (from bottom to top with increasing U_h). The blue thin curves are the same but predictions including the PDR component with $\gamma = 0.04$, for several values of U_{\min} . The dotted curves are the corresponding PDR components. The dashed curves are predictions by the DH02 model for the four values of α_{DH} (from top to bottom with increasing α_{DH}). The dot-dashed curves are the $\beta = 1.75$ modified blackbody spectra for several values of dust temperature T_d (from bottom to top with increasing T_d).

3.2. Fitting to the AKARI/FIS Data

Because the number of galaxies detected by IRC is small and we concentrate on U_h for the broad thermal peak in SEDs, we use only the four AKARI/FIS bands in the SED fits. For a galaxy whose energy flux per unit frequency is $F_\nu(\nu)$, the i -th FIS band flux quoted in the FIS-BSC catalog (in units of Jy) is calculated as

$$F_i = \frac{1}{\Delta\nu_i} \int d\nu F_\nu(\nu) R_i(\nu), \quad (5)$$

where ν is the frequency in the observer's frame, $\Delta\nu_i$ is the band width

$$\Delta\nu_i \equiv \nu_c \int d\nu \nu^{-1} R_i(\nu), \quad (6)$$

$\nu_c = c/\lambda_c$ is the central frequency of the band given in Table 1, and $R_i(\nu)$ is RSRF against energy flux for each AKARI band shown in Fig. 1. The band width is defined so that $F_i = F_\nu(\nu_c)$ when $\nu F_\nu(\nu)$ is constant. The observed energy flux is related to luminosity $L_\nu(\nu_r; M_{\text{DIR}}, U_h)$ of the DL07 model per unit rest-frame frequency at a redshift z as

$$F_\nu(\nu) = \frac{(1+z)}{4\pi d_L(z)^2} L_\nu(\nu_r; M_{\text{DIR}}, U_h), \quad (7)$$

where the rest-frame frequency is $\nu_r = (1+z)\nu$.

Then the best-fit values of M_{dIR} and U_h are calculated by the standard χ^2 minimization, i.e.,

$$\chi^2(M_{\text{dIR}}, U_h) = \sum_{i=1}^4 \frac{[F_i^{\text{obs}} - F_i^{\text{model}}(M_{\text{dIR}}, U_h)]^2}{(\Delta F_{\text{tot},i})^2}, \quad (8)$$

where the summation is over the four FIS bands. When the flux measurement is not reported for a FIS band in the FIS-BSC catalog, this band was not used in the fitting. The number of the FIS bands used for a fitting to a galaxy is denoted by N_{dat} , and because of our requirement of $FQUAL \geq 3$ at least in two of the four FIS bands, $2 \leq N_{\text{dat}} \leq 4$. There are 3, 44, and 831 galaxies having $N_{\text{dat}} = 2-4$ for the AKARI-SDSS sample and 4, 33, and 674 for the AKARI-HIPASS sample, respectively. The range of U_h covered in the fittings is $0.1 \leq U_h \leq 10^3$, where the lower bound is limited by the available model library, and the upper bound is large enough because we found no galaxies having $U_h > 100$. There are 20 and 24 galaxies whose best-fit U_h is 0.1 (the lower bound of the model) for the AKARI-SDSS and AKARI-HIPASS samples, respectively, and the following statistical analyses are not significantly affected by these small number of galaxies. The total infrared luminosity L_{TIR} is then calculated as the bolometric luminosity of the dust emission from the best-fit SED model.

The 1σ error ΔU_h for U_h was calculated for each galaxy by the range corresponding to $\Delta\chi^2 = 1$ from the χ^2 minimum, taking the best-fit normalization (i.e., M_{dIR}) for each value of U_h . The errors of M_{dIR} and L_{TIR} are correlated with U_h , and we estimated them as follows. For a fixed value of U_h , the error for the normalization factor can be estimated as (see, e.g., Press et al. 2007)

$$\frac{\Delta M_{\text{dIR}}}{M_{\text{dIR}}} = \frac{\Delta L_{\text{TIR}}}{L_{\text{TIR}}} = \frac{1}{M_{\text{dIR}}} \left(\frac{1}{2} \frac{\partial^2 \chi^2}{\partial M_{\text{dIR}}^2} \right)^{-\frac{1}{2}}. \quad (9)$$

In addition, to take into account the error correlated with U_h , we calculated the change of best-fit M_{dIR} and L_{TIR} values when U_h is changed from the best-fit value by $\pm\Delta U_h$. Then the quadratic sum of these two types of errors was calculated as the final error for M_{dIR} and L_{TIR} . We found that the mean errors of $\log_{10} U_h$ and $\log_{10} M_{\text{dIR}}$ are ~ 0.17 both for the AKARI-SDSS and AKARI-HIPASS samples, and that for $\log_{10} L_{\text{TIR}}$ is smaller than these by a factor of about four. The error of L_{TIR} is small because it is directly connected to the observed fluxes, while M_{dIR} and U_h have similar fractional uncertainties about the SED shape by the relation $L_{\text{TIR}} \propto M_{\text{dIR}} U_h$.

Six examples of the fittings to the AKARI-SDSS galaxies are shown in Fig. 12. The distributions of U_h and the minimum reduced chi-square, $\chi_{\text{red}}^2 \equiv \chi^2/\nu$ for $N_{\text{dat}} \geq 3$ galaxies are shown in Fig. 13, where the degree of freedom is $\nu = N_{\text{dat}} - 2$ for the two-parameter fittings. Theoretical expectations of the χ_{red}^2 distribution (weighted sum of those for $N_{\text{dat}} = 3$ and 4) are also shown. The observed χ_{red}^2 distribution is larger than the ideal theoretical prediction by a factor of ~ 1.5 , but we consider that this is not unreasonable, if we take into account the possible sys-

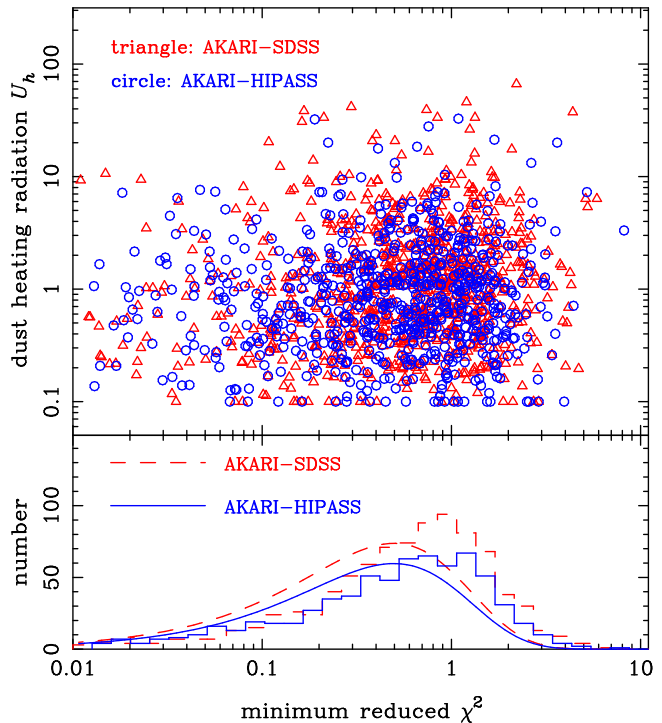


Fig. 13. (Top) Dust-heating radiation field strength (U_h) versus the minimum reduced chi-square (χ_{red}^2) of SED fittings for the AKARI-SDSS and AKARI-HIPASS samples. (Bottom) The histogram of the minimum χ_{red}^2 . The curves are the theoretically expected distribution from the χ^2 statistics for $\nu = (N_{\text{dat}} - 2)$ degrees of freedom. Only galaxies with $N_{\text{dat}} \geq 3$ are shown in this figure.

tematic errors in the AKARI flux calibration and/or the possible difference of the single- U DL07 model from the reality.

3.3. Models versus Observations in the IRC Bands

In this paper we will concentrate on the SED parameter U_h determined by fits to the AKARI/FIS bands, but it would also be interesting to compare the observed AKARI/IRC fluxes with those predicted by the physical dust models. This is done in Fig. 14, where we show the flux ratios of F_{18}/F_{90} and F_9/F_{18} against F_{90}/F_{140} , where F_x denotes the AKARI photometric flux of the x - μm band. Here we have used galaxies with the AKARI/FIS flux quality flag $FQUAL \geq 3$ both in the 90- and 140- μm bands from the AKARI-SDSS and AKARI-HIPASS samples. The ratio of F_{90}/F_{140} can be regarded as an indicator of the dust temperature or U_h . The solid curves are the path along U_h predicted by the single- U DL07 model, and the prediction for F_{18}/F_{90} is lower than the mean of the observed distribution by a factor of about two. This is reasonable because mid-infrared emission is likely dominated by dust grains in regions of stronger heating radiation field, and we must incorporate the diversity of U to fit SEDs in a wide wavelength range. Here we adopt two such SED models.

One is the physical dust model by Dale & Helou (2002, hereafter DH02), which introduces a power-law distribu-

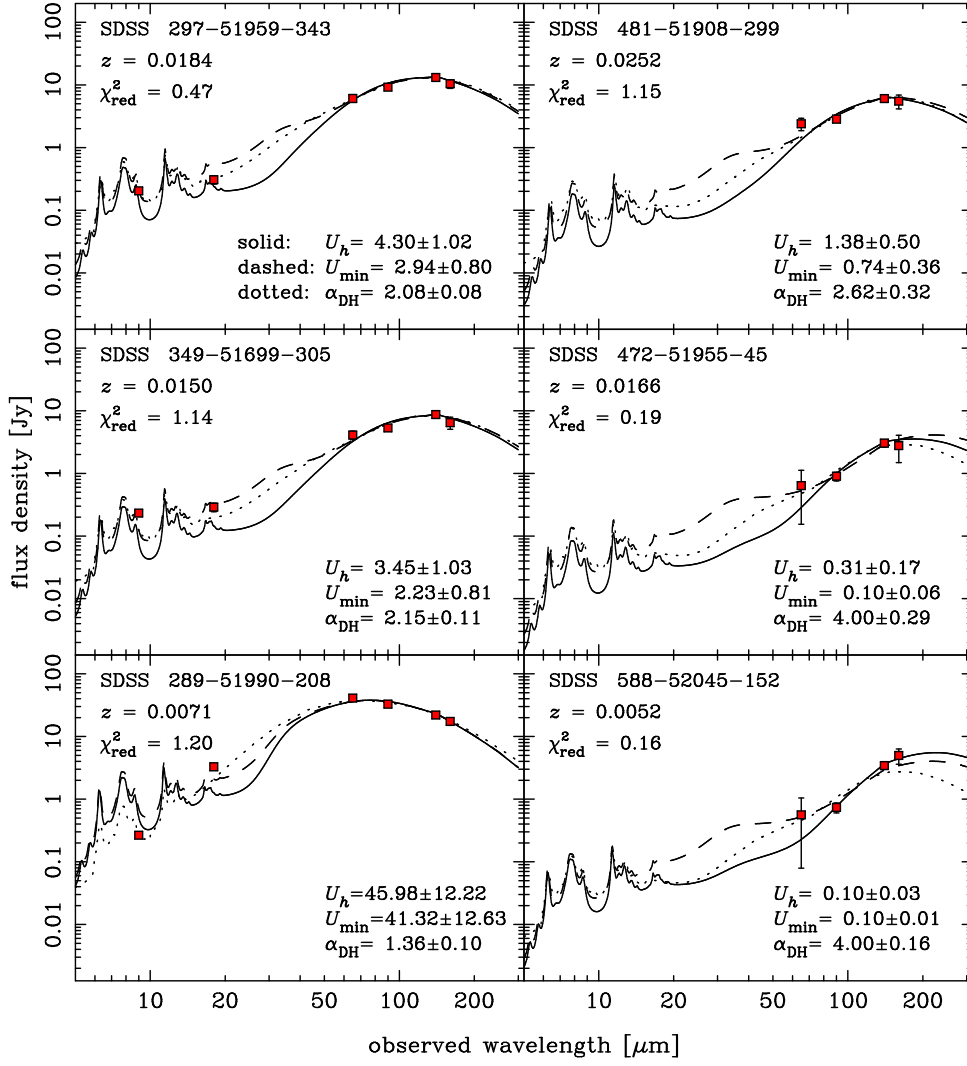


Fig. 12. Examples of the SED fittings to the galaxies in the AKARI-SDSS sample. The squares are AKARI data points, and error bars are small and difficult to see for most of them. The three different models are used for the fits: the $\gamma = 0$ DL07 model with the parameter U_h (solid), the $\gamma = 0.04$ DL07 model with the parameter U_{min} (dashed), and the DH02 model with the parameter α_{DH} (dotted). The best-fit parameters and $\chi^2_{\text{red}} = \chi^2/\nu$ (with $\nu = N_{\text{dat}} - 2$ degrees of freedom, for the $\gamma = 0$ DL07 model) are shown in each panel. The unique identification set of plate number, MJD, and fiber number of the SDSS spectroscopic database is also shown in each panel.

tion of radiation strength as

$$\frac{dM_{\text{dIR}}}{dU} \propto U^{-\alpha_{\text{DH}}}, \quad (10)$$

and the path along α_{DH} predicted by this model is shown in Fig. 14. The values of $\alpha_{\text{DH}} = 4, 3, 1.8,$ and 1 roughly correspond to $U_h = 0.6, 1.0, 10,$ and 100 of the single- U DL07 model, respectively, in our SED fits to the four FIS bands. This model shows a better agreement with the data than the single- U DL07 model, demonstrating the necessity of including a small amount of large U dust component. On the other hand, the data show dispersions by about one order of magnitude in both the flux ratios of F_9/F_{18} and F_{18}/F_{90} , indicating the limitation of one-parameter-family SED models. The SEDs of the DH02 model are also shown in Figs. 11 and 12.

The other model is DL07 using a form of dM_{dIR}/dU

proposed by DL07, which introduces a power-law distribution of dM_{dIR}/dU in the range of $U_{\text{min}} \leq U \leq U_{\text{max}}$ for a fraction γ of the total dust mass, in addition to the single- U component with $U = U_{\text{min}}$, i.e.,

$$\begin{aligned} \frac{dM_{\text{dIR}}}{dU} = & (1 - \gamma) M_{\text{dIR}} \delta(U - U_{\text{min}}) \\ & + \gamma M_{\text{dIR}} \frac{\alpha - 1}{U_{\text{min}}^{1-\alpha} - U_{\text{max}}^{1-\alpha}} U^{-\alpha}. \end{aligned} \quad (11)$$

The power-law component is called as the PDR component as it represents the hot dust in photodissociation regions (PDRs) close to young massive stars. We adopt $\alpha = 2$ and $U_{\text{max}} = 10^6$ for the PDR component following Draine et al. (2007), and now we have another model parameter γ in addition to U_{min} . (The model has yet another degree of freedom about the PAH fraction by the model parameter j_M , but we keep $j_M = 5$ to reduce the param-

eter space to explore.) The PDR component models are available only for $U_{\min} \leq 25$, and we use the $U_{\min} = 25$ template for the PDR component when $U_{\min} > 25$. We calculated the path along U_{\min} in the plane of F_{90}/F_{140} versus F_9/F_{18} and F_{18}/F_{90} for various values of γ , and found that $\gamma = 0.04$ gives the median of the observed distribution, as shown in Fig. 14. This value is close to the typical value found by Drain et al. (2007) for nearby galaxies, though there is a significant scatter of γ . The SED model curves of the $\gamma = 0.04$ model are also shown in Figs. 11 and 12.

Although the $\gamma = 0.04$ model is better than the single- U model (i.e., $\gamma = 0$) to reproduce the observed IRC fluxes, we will use the latter in the analyses below because of the following reasons. First of all, we want to estimate the characteristic radiation field strength U_h responsible for the emission around the thermal peak from large dust grains, and introducing the PDR component in a model-dependent way may induce some bias in the estimates of U_h . The $\gamma = 0.04$ model produces a feature around $30 \mu\text{m}$ because of the rather arbitrary parameter of $U_{\max} = 10^6$, when U_{\min} is small. The best-fit U_{\min} values of the $\gamma = 0.04$ model tend to be smaller than U_h of the $\gamma = 0$ model (see Fig. 12), and we found that a considerable number of galaxies have the lowest value of $U_{\min} = 0.1$ provided in the model library. The number of such galaxies can be minimized by using the $\gamma = 0$ model. Finally, it should also be noted that the deficit of the predicted IRC-band flux by the $\gamma = 0$ model is at most a factor of two compared with the mean observed flux.

4. Theoretical Considerations

Before we compare the infrared SED parameters with other physical quantities of galaxies, we describe the general theoretical expectations. The basic assumptions here are that dust and heating radiation sources are uniformly distributed on a disk (but possibly with different scale heights). This picture is obviously simple, and allowed only when the infrared SED is determined mostly by the general ISRF on the global scale in a galaxy, rather than those associated with small scale structures like individual star forming regions. However, rather surprisingly, we will find that this simple picture gives reasonable explanations for most of the data presented in the paper, and more geometrically complex models are not warranted.

4.1. Basic Equations of Emission from Dust

The infrared SED depends on the heating radiation field strength felt by dust particles, which is defined by the energy density u_ν or energy flux s_ν per unit frequency, and these two are simply related as $s_\nu = c u_\nu$, where c is the speed of light. The radiation field can be anisotropic, but anisotropy does not affect the infrared emission from heated dust, and these quantities are defined as those integrated over 4π steradians. In this work we do not consider the variation of the SED of the heating radiation field, and use the same parameter U_h introduced in §3, which is a dimensionless field strength normalized by the local strength

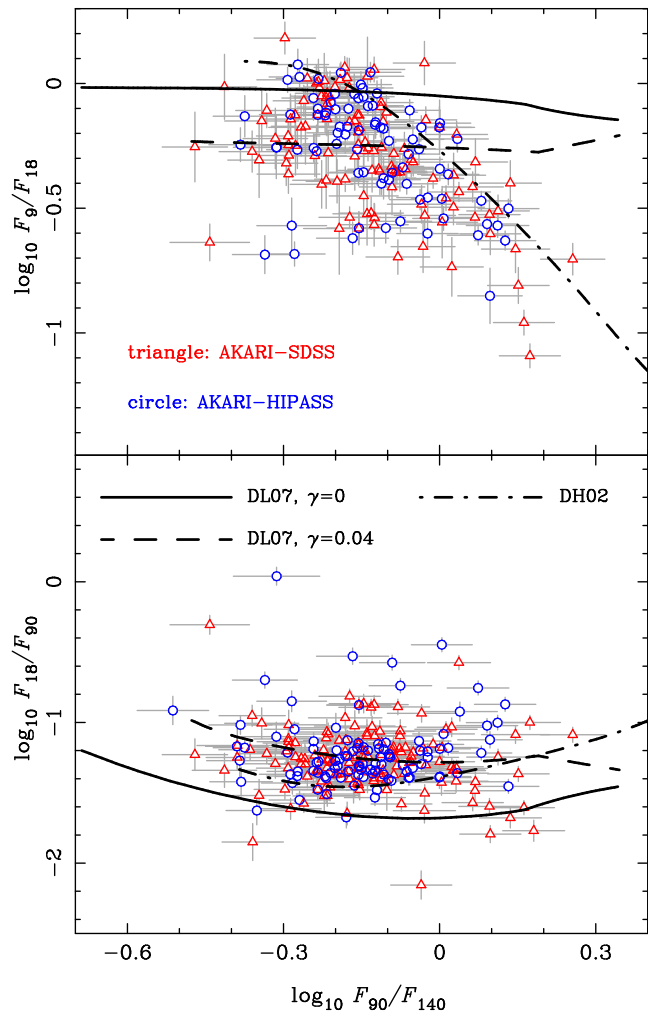


Fig. 14. The color index correlations for the AKARI-SDSS and AKARI-HIPASS samples. The flux F_x denotes photometric flux in the AKARI x - μm band in units of Jy. The three curves are the predicted path along the model parameters by the physical dust models. The solid, dashed, and dot-dashed curves are for the $\gamma = 0$ DL07 model ($U_h = 0.1$ –100), the $\gamma = 0.04$ DL07 model ($U_{\min} = 0.1$ –100), and the DH02 model ($\alpha_{\text{DH}} = 0.0625$ –4), respectively. The model predictions assume $z = 0.02$ that is typical for the observed galaxies.

$u_{\nu,0}$ of the Milky Way ISRF around the solar neighbourhood, i.e., $u_{\nu}(\nu) = U_h u_{\nu,0}(\nu)$ and $s_{\nu}(\nu) = U_h s_{\nu,0}(\nu)$.

When dust particles of total mass M_{dIR} are exposed to a heating radiation field strength U_h and emitting in a stationary state (a good approximation in the AKARI/FIS bands), the bolometric luminosity L_{TIR} emitted from these particles is given by the energy balance with the total energy absorbed by dust grains, as

$$L_{\text{TIR}} = M_{\text{dIR}} \int d\nu \kappa_d(\nu) s_{\nu}(\nu) \quad (12)$$

$$= M_{\text{dIR}} U_h \int d\nu \kappa_d(\nu) s_{\nu,0}(\nu), \quad (13)$$

where κ_d is the dust mass opacity coefficient (absorption cross section per unit mass of dust grains, see, e.g., Hildebrand 1983; Dunne et al. 2003). If we define the frequency-integrated effective dust mass opacity weighted by $s_{\nu,0}$, as

$$\kappa_{d,\text{eff}} \equiv \frac{\int d\nu \kappa_d(\nu) s_{\nu,0}(\nu)}{\int d\nu s_{\nu,0}(\nu)}, \quad (14)$$

we obtain

$$L_{\text{TIR}} = \kappa_{d,\text{eff}} M_{\text{dIR}} U_h s_{\text{bol},0}, \quad (15)$$

where $s_{\text{bol},0} \equiv \int s_{\nu,0} d\nu$ is the bolometric intensity of the local ISRF, for which we adopt the value of Mathis et al. (1983): $s_{\text{bol},0} = 0.0259 \text{ erg cm}^{-2} \text{ s}^{-1}$ in 0–13.6 eV (see also Draine et al. 2007). We can calculate $\kappa_{d,\text{eff}}$ for the physical dust model of DL07 from eq. (15), which is found to be $\kappa_{d,\text{eff}} = 1.0 \times 10^4 \text{ cm}^2 \text{ g}^{-1}$. In astronomically convenient units, this can also be written as

$$\frac{L_{\text{TIR}}}{L_{\odot}} = 1.4 \times 10^2 \frac{M_{\text{dIR}}}{M_{\odot}} U_h. \quad (16)$$

Now, adopting the disk geometry, we define the global infrared radiation field strength of a galaxy by

$$\Sigma_{\text{TIR}} \equiv \frac{1}{2} \frac{L_{\text{TIR}}}{\pi R^2} = \frac{1}{2} \kappa_{d,\text{eff}} \Sigma_{\text{dIR}} U_h s_{\text{bol},0}, \quad (17)$$

where R is the characteristic disk radius of a galaxy, and the dust mass column density of a galactic disk is defined as $\Sigma_{\text{dIR}} \equiv M_{\text{dIR}}/(\pi R^2)$. In this work we use the 90% Petrosian radius R_{P90} as R for the AKARI-SDSS and AKARI-HIPASS samples, which includes most of the total luminosity from a galaxy. For the AKARI-SB galaxies, we use the size of circumnuclear starburst regions given in K98. The factor of 1/2 is introduced to approximately account for the disk geometry where the radiation is emitted into the two sides of the disk. The quantity Σ_{TIR} has the same physical dimension as the heating radiation field strength $s_{\text{bol}} = U_h s_{\text{bol},0}$, and we expect some relation between the two if the infrared emission is mainly determined by the global properties of a galaxy. To directly compare with the dimensionless strength U_h , we normalize Σ_{TIR} as

$$U_{\text{TIR}} \equiv \frac{\Sigma_{\text{TIR}}}{s_{\text{bol},0}} = \frac{1}{2} \kappa_{d,\text{eff}} \Sigma_{\text{dIR}} U_h. \quad (18)$$

The effective optical depth $\tau_{d,\text{eff}}$ of dust, corresponding to the light travel distance l , is defined as $\tau_{d,\text{eff}} = \kappa_{d,\text{eff}} \rho_d l$,

where ρ_d is the spatial mass density of dust in ISM. The optical depth is related to dust mass column density and V band extinction as:

$$\tau_{d,\text{eff}} = \left(\frac{\rho_d l}{\kappa_{d,\text{eff}}^{-1}} \right) = 0.327 A_V, \quad (19)$$

where $\kappa_{d,\text{eff}}^{-1} = 0.48 M_{\odot} \text{ pc}^{-2}$ and we have used the relation between A_V and hydrogen column density, $A_V/N_{\text{H}} = 5.3 \times 10^{-22} \text{ mag cm}^2 (\text{H atom})^{-1}$, for the DL07 physical dust model. We also introduce the total optical depth $\tau_{d,\text{eff}}^{\text{tot}}$ of the disk, which is defined as

$$\tau_{d,\text{eff}}^{\text{tot}} \equiv \frac{1}{2} \frac{\kappa_{d,\text{eff}} M_d}{\pi R^2} = \frac{1}{2} \kappa_{d,\text{eff}} \Sigma_d = \frac{\Sigma_d}{\Sigma_{d,\text{crit}}}, \quad (20)$$

where M_d is the total dust mass in a galaxy, $\Sigma_d \equiv M_d/(\pi R^2)$, and we have defined the critical dust mass column density $\Sigma_{d,\text{crit}} \equiv 2\kappa_{d,\text{eff}}^{-1} = 0.96 M_{\odot} \text{ pc}^{-2}$ for which $\tau_{d,\text{eff}}^{\text{tot}} = 1$. The factor 1/2 has been introduced because, on average, radiation from heating sources passes through about half of the total column density of the dust disk. It should be noted that here we make a distinction between M_{dIR} (heated dust mass estimated from infrared emission) and the total dust amount M_d in a galaxy. Generally M_{dIR} (or Σ_{dIR}) can be smaller than M_d (or Σ_d), if only a fraction of dust particles are radiated by strong radiation field. The total disk optical depth $\tau_{d,\text{eff}}^{\text{tot}}$ is defined by M_d rather than M_{dIR} . Then we have

$$U_{\text{TIR}} = \tau_{d,\text{eff}}^{\text{tot}} \frac{\Sigma_{\text{dIR}}}{\Sigma_d} U_h = \tau_{d,\text{eff}}^{\text{tot}} \frac{M_{\text{dIR}}}{M_d} U_h. \quad (21)$$

This is an important equation that will be used to interpret the observed data in this work.

4.2. Scalings among U_{TIR} , U_h , M_{dIR} , and M_d

Eq. (21) is a generic equation, but we can consider some limiting cases with simple scaling laws, corresponding to a particular geometrical distribution of dust and heating sources. The schematic picture to explain these cases is given in Fig. 15.

First we consider the case of small optical depth, $\tau_{d,\text{eff}}^{\text{tot}} \ll 1$ (hereafter the case A). In this case the heating radiation field strength should be $s_{\text{bol}} = U_h s_{\text{bol},0} \sim L_h/(2\pi R^2)$, where L_h is the bolometric luminosity of heating radiation from all sources in a galaxy. This field strength is relevant for all dust particles in a galaxy, and hence $M_{\text{dIR}} \sim M_d$, while only a small fraction of the heating radiation energy is absorbed and converted into the infrared emission, i.e., $U_{\text{TIR}} \sim \tau_{d,\text{eff}}^{\text{tot}} U_h < U_h$.

In the opposite limit of large optical depth ($\tau_{d,\text{eff}}^{\text{tot}} \gg 1$), most of heating radiation will be converted into infrared emission, and hence $L_{\text{TIR}} \sim L_h$ and $\Sigma_{\text{TIR}} \sim L_h/(2\pi R^2)$ (hereafter the case B). We can further consider two very different limiting cases about the relative distributions of dust and heating sources. The first case is when dust particles have a similar disk scale height as the heating sources. Then all the dust particles in the disk contribute in the same way to the infrared emission, i.e., $M_{\text{dIR}} = M_d$. Then eq. (21) tells us $U_{\text{TIR}} = \tau_{d,\text{eff}}^{\text{tot}} U_h$, i.e., $U_{\text{TIR}} > U_h$,

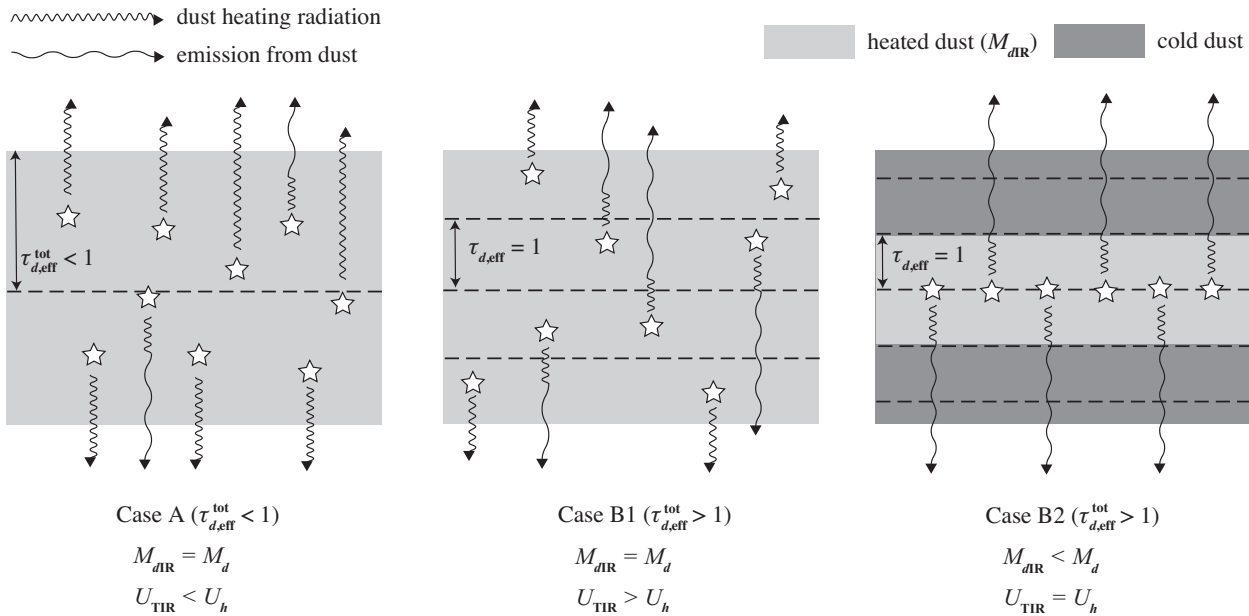


Fig. 15. Schematic pictures for the representative cases of the geometrical distributions of dust-heating stars and dust grains, in the disk geometry. The normal of the disk plane is along the vertical direction.

meaning that the heating radiation strength felt by dust particles (U_h) is smaller than $U_{\text{TIR}} = L_h/(2\pi R^2 s_{\text{bol},0})$ by a factor of $\tau_{d,\text{eff}}^{\text{tot}}$. This is because the heating photons are substantially absorbed after traveling through a distance corresponding to $\tau_{d,\text{eff}} = 1$, and only a fraction ($\sim 1/\tau_{d,\text{eff}}^{\text{tot}}$) of total heating radiation produced in the disk reaches a dust particle. We call this as the case B1.

Another optically thick case is when the disk scale height of heating sources is smaller than that of dust particles. As a simple example, we assume that the scale height of heating sources is negligibly small, so that the dust disk behaves like an optically thick screen. Then the radiation field strength at regions close to the heating sources should be $s_{\text{bol}} = L_h/(2\pi R^2) = \Sigma_{\text{TIR}}$, i.e., $U_h = U_{\text{TIR}}$. Then eq. (21) requires

$$\frac{\Sigma_{\text{dIR}}}{\Sigma_d} = \frac{M_{\text{dIR}}}{M_d} = \frac{1}{\tau_{d,\text{eff}}^{\text{tot}}}, \quad (22)$$

meaning that only a fraction ($\sim 1/\tau_{d,\text{eff}}^{\text{tot}}$) of dust particles are heated by the radiation, because the radiation field is significantly damped after traveling through a distance corresponding to $\tau_{d,\text{eff}} = 1$. Infrared emission is mostly from the dust in the thin layer corresponding to $\tau_{d,\text{eff}} \sim 1$ around the heating sources. Then it is predicted that the column density of heated dust is constant at $\Sigma_{\text{dIR}} \sim \Sigma_{d,\text{crit}}$, regardless of the total dust column density Σ_d . We call this as the case B2.

Note that $M_{\text{dIR}} \sim M_d$ and $U_{\text{TIR}} \sim U_h$ can be realized simultaneously only when $\tau_{d,\text{eff}}^{\text{tot}} \sim 1$.

5. Results and Interpretation

Here we present the main results of this work, i.e., the correlation between infrared SEDs and various physical

properties of galaxies. The results will be interpreted by the theoretical background described in the previous section.

5.1. Infrared Luminosity versus Optical Luminosity and SFR

First we compare the infrared luminosity L_{TIR} with the optical luminosity, to examine the dust opacity $\tau_{d,\text{eff}}^{\text{tot}}$. Figure 16 shows the correlation between L_{TIR} and the optical r -band luminosity ($L_r \equiv \nu L_\nu$ at rest-frame 6231 Å). We find $L_{\text{TIR}} \gtrsim L_r$ for most galaxies, indicating that energy output by dust emission is similar to, or larger than that by the direct stellar emission. It may indicate that most galaxies have $\tau_{d,\text{eff}}^{\text{tot}} \gtrsim 1$, but we can derive this conclusion only if the L_{TIR}/L_r ratio is determined by the global properties of galaxies, because $\tau_{d,\text{eff}}^{\text{tot}}$ has been defined as the mean dust column density on a galactic scale. Instead, the L_{TIR}/L_r ratio may be determined by the properties of local star forming regions in a galaxy. We will find that the former interpretation, $\tau_{d,\text{eff}}^{\text{tot}} \gtrsim 1$, is indeed appropriate for the galaxies studied here.

Next we examine the correlation between L_{TIR} and SFR (ψ , estimated from SDSS spectra) of the AKARI-SDSS sample, shown in the left panel of Figure 17, to examine the origin of dust heating radiation. The total infrared luminosity L_{TIR} is often used as a SFR indicator by eq. (4), and its validity and limitation have been discussed in the literature (e.g., Takeuchi et al. 2005, Salim et al. 2009; Boquien et al. 2010; Goto et al. 2011b). It cannot be a good SFR indicator when star formation activity is low and dust heating radiation is significantly contributed from relatively aged stars. This trend is clearly seen in this figure; L_{TIR}/ψ increases with decreasing SFR. The solid line is the L_{TIR}/ψ ratio of eq. (4), which is the

value expected when the dust heating radiation is dominated by young stellar populations with ages of 10–100 Myr (Kennicutt 1998, converted to the Kroupa IMF here). This L_{TIR}/ψ ratio is observed only for high SFR galaxies. Different symbols are used in this figure for different ranges of L_{TIR}/L_r , and the trend of larger L_{TIR}/L_r for larger SFR can be seen, in agreement with the well-known fact that actively star-forming galaxies are generally dusty.

Since SSFR ($\psi_s \equiv \psi/M_*$) is a good measure of relative abundances of young and old stellar populations, we expect that L_{TIR}/ψ is tightly correlated with SSFR. This is indeed seen in the right panel of Figure 17, especially for galaxies having $L_{\text{TIR}}/L_r < 10$. On the other hand, dusty galaxies having $L_{\text{TIR}}/L_r > 10$ deviate from the correlation showing particularly high L_{TIR} , and this is most likely explained by the hidden activity of star formation that cannot be captured by optical emission because of large extinction. The tight correlation of galaxies with $L_{\text{TIR}}/L_r < 10$ can be fit as

$$\frac{L_{\text{TIR}}}{\psi} = 4.0 \left(\frac{\psi_s}{\text{Gyr}^{-1}} \right)^{-0.54} L_{\odot} M_{\odot}^{-1} \text{Gyr}. \quad (23)$$

This result indicates that SSFR can be used as an indicator of contribution from young stellar population to dust-heating radiation. The infrared luminosity L_{TIR} can be used as a simple SFR indicator only for actively star-forming galaxies of $\psi_s \gtrsim 0.1 \text{ Gyr}^{-1}$, while for other galaxies relatively aged stars significantly contribute to the dust-heating radiation. The tight L_{TIR}/ψ versus ψ_s correlation may be useful for parameter estimations for observed galaxies, because if two of the three parameters (M_* , SFR, and L_{TIR}) are known, the remaining parameter can be deduced by solving the $L_{\text{TIR}}/\psi - \psi_s$ relation. For example, if one knows L_{TIR} and M_* from observations, SFR can be solved from this relation, which should be a better estimation than simply using eq. (4).

5.2. Infrared SED versus Infrared Luminosity and SSFR

Figure 18 shows the correlation between L_{TIR} and U_h , for the AKARI-SDSS and AKARI-HIPASS samples. As mentioned in §1, the correlation between the two (larger U_h for larger L_{TIR}) is widely known, and the trend is also confirmed for both the two samples studied here. However, there is a considerable scatter and it is difficult to predict U_h with a good accuracy only by the information of L_{TIR} . Furthermore, we find a significant offset of the mean relation between the two sample. Since the AKARI-SDSS galaxies are more distant, their mean L_{TIR} is larger than that of the AKARI-HIPASS galaxies, but the distribution of U_h is not significantly different. This indicates that the $L_{\text{TIR}}-U_h$ or $L_{\text{TIR}}-T_d$ relation is sensitive to the sample selections.

Figure 19 shows the correlation between L_{TIR} and α_{DH} of the DH02 model fits. It is interesting to compare the α_{DH} distribution of our samples with that of the IRAS $F_{60} > 1.2 \text{ Jy}$ sample (Fisher et al. 1995). Converting the distribution of F_{60}/F_{100} flux ratio of this sample given in Chapman et al. (2003) into α_{DH} using the relation

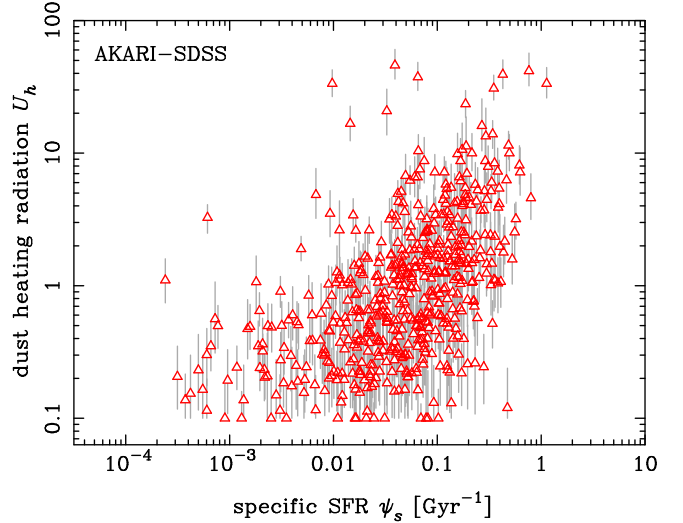


Fig. 20. Dust-heating radiation strength (U_h , estimated by infrared SED fittings) versus specific star formation rate ($\psi_s \equiv \psi/M_*$, ψ and M_* from SDSS spectra) for the AKARI-SDSS sample.

in Table 2 of Dale et al. (2001)⁵, the mean is $\alpha_{\text{DH}} \sim 2$ and there are few galaxies having $\alpha_{\text{DH}} > 2.5$ in this IRAS-based sample. This is in contrast to the AKARI-SDSS and AKARI-HIPASS samples that include many galaxies at $\alpha_{\text{DH}} > 2.5$. This is likely because the IRAS sample was selected at the IRAS 60- μm band, while many of the galaxies in our sample are detected in the AKARI 90- and 140- μm bands with the FIS flux quality flag $FQUAL \geq 3$ (see Table 3). Therefore our samples include galaxies having colder dust temperatures than the IRAS-based sample. Note that the errors of α_{DH} (calculated in the same way as U_h) are large when $\alpha_{\text{DH}} \gtrsim 3$, because the dependence on α_{DH} of the DH02 templates becomes weaker.

Figure 20 shows the correlation between SSFR and U_h for the AKARI-SDSS sample, using SDSS SFR and stellar mass. This correlation is physically more reasonable than $L_{\text{TIR}}-U_h$, because both SSFR and U_h are intensive physical quantities (i.e., not depending on the system size or the amount of material). In fact, we see a better correlation in Fig. 20 than the $L_{\text{TIR}}-U_h$ correlation: larger U_h for galaxies having larger SSFR. However the slope of the correlation becomes steeper at $\psi_s \gtrsim 0.1 \text{ Gyr}^{-1}$, and it is still difficult to predict U_h reliably simply from SSFR. It should also be noted that SSFR is not a directly observable quantity, and physical relation between SSFR and U_h is not clear. SSFR is related to star formation history in a galaxy and hence it would affect the SED of dust-heating radiation field. However, a key quantity controlling the radiation field strength is the geometrical size, which is not directly related with SSFR. Correlations between U_h and more directly observable quantities based on better physical connections are worth to seek for.

⁵ Here we ignored the K -correction, which is a good approximation for the low-redshift sample.

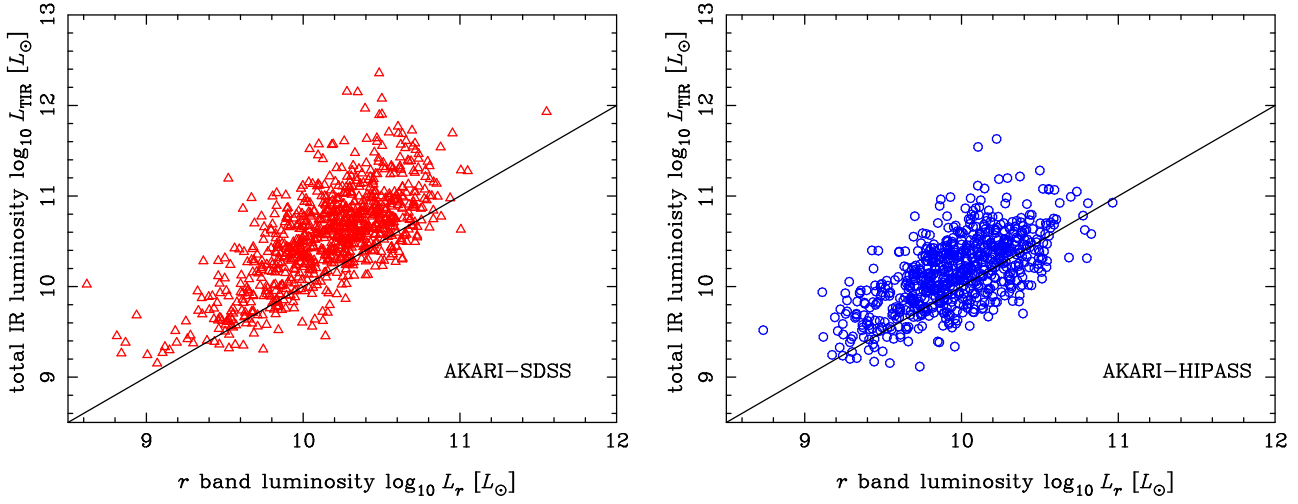


Fig. 16. Total infrared luminosity (L_{TIR}) versus optical luminosity L_r (νL_ν at the rest-frame r band) of the AKARI-SDSS and AKARI-HIPASS samples.

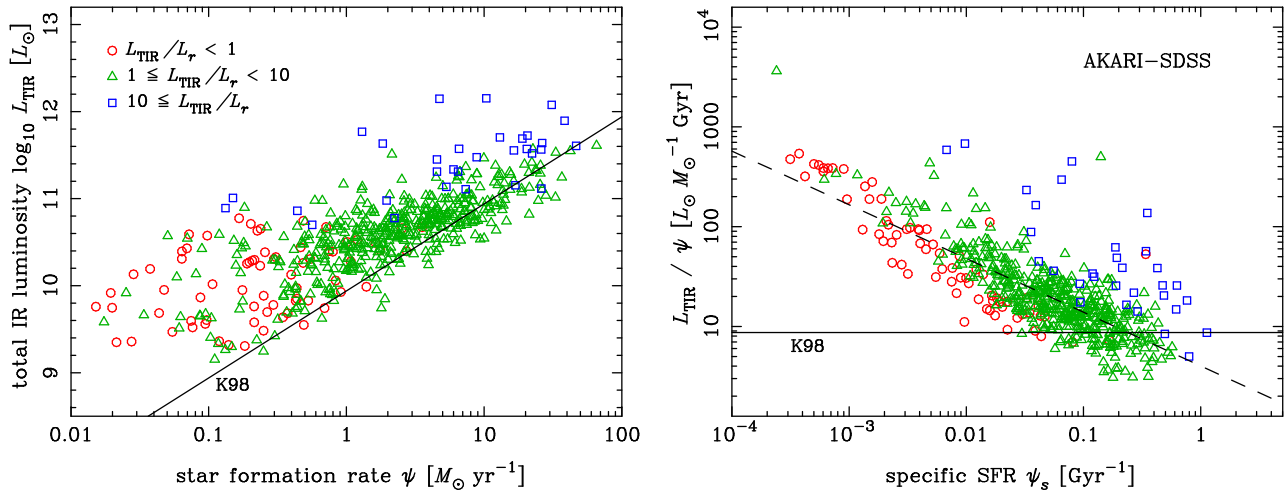


Fig. 17. Correlation between SFR (ψ , estimated by SDSS spectra) and L_{TIR} (left), and that between SSFR ($\psi_s \equiv \psi/M_*$) and L_{TIR}/ψ (right) for the AKARI-SDSS sample. Different symbols are used for different ranges of the infrared-to-optical luminosity ratio, L_{TIR}/L_r , as shown in the left panel. The solid lines are the calibration of L_{TIR}/ψ by Kennicutt (1998), but corrected for the Kroupa IMF for L_{TIR} as an SFR indicator. The dashed line in the right panel is the best-fit power-law to the galaxies with $L_{\text{TIR}}/L_r < 10$.

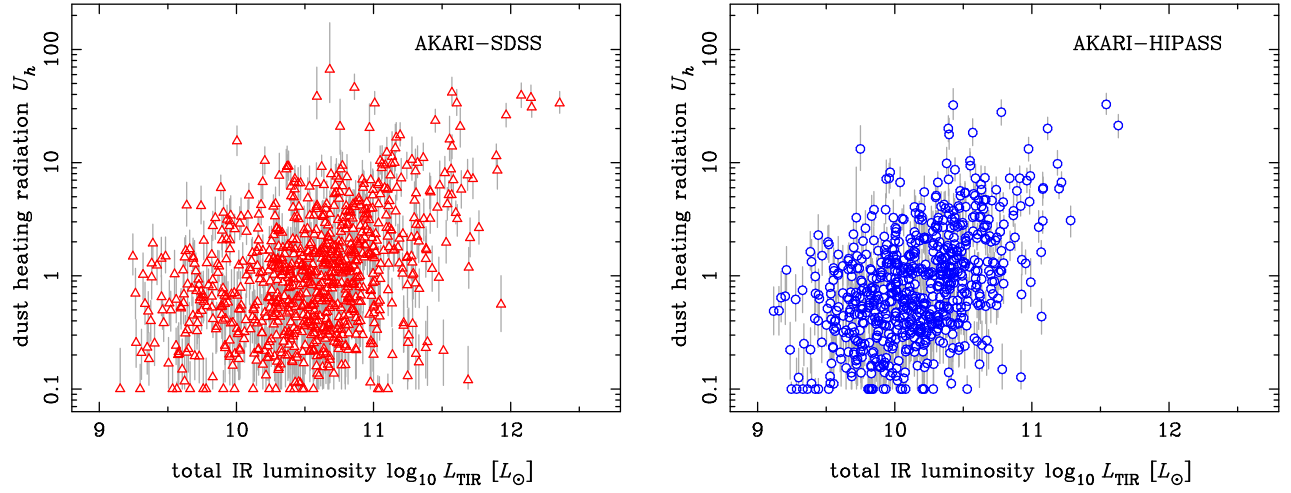


Fig. 18. Dust-heating radiation field strength (U_h , estimated by infrared SED fittings) versus total infrared luminosity L_{TIR} , for the AKARI-SDSS (left) and AKARI-HIPASS (right) samples.

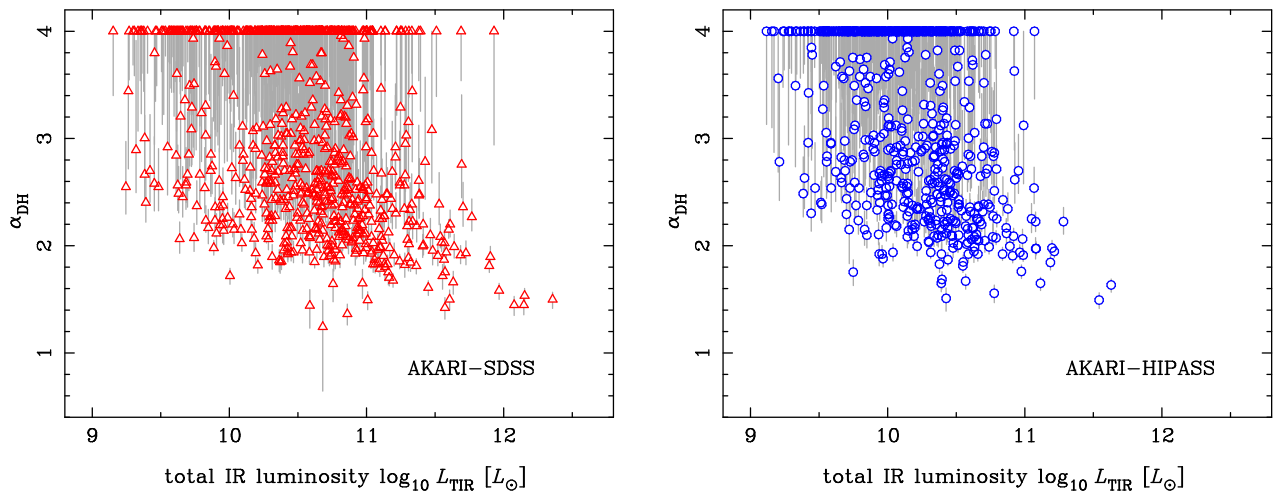


Fig. 19. The same as Fig. 18, but for the correlation of α_{DH} (obtained by the SED fittings with the DH02 model) versus L_{TIR} .

5.3. Infrared SED versus Global Infrared Radiation Field Strength

Figure 21 shows the correlation between U_h and U_{TIR} , i.e., the galactic-scale infrared radiation field strength $\Sigma_{\text{TIR}} \equiv L_{\text{TIR}}/(2\pi R^2)$ normalized by the solar neighbourhood value of ISRF. It can be seen that these two parameters are correlated much better than the $L_{\text{TIR}}-U_h$ or ψ_s-U_h relations. The relation is well described by the linear relation of $U_h \propto U_{\text{TIR}}$, with the ratio $U_h/U_{\text{TIR}} \sim 1$. This result is in nice agreement with the prediction in the case B2 discussed in §4.2, and it strongly indicates that (1) integrated infrared SED of a galaxy is mostly determined by the general ISRF on the global scale of a galaxy, and (2) dust-heating sources are deeply embedded in an optically-thick dust disk, i.e., the scale height of heating sources being smaller than one optical depth of the dust disk.

There are several independent observational evidences supporting this picture. Walterbos & Greenawalt (1996) and Sun & Hirashita (2010) argued for the dominant role of the general ISRF in the determination of infrared SEDs. The geometry of the case B2 is consistent with the smaller scale height of molecular gas than that of HI in the Galaxy (Malhotra 1994, 1995; Binney & Merrifield 1998), considering that young stars are generally born in dense molecular gas. Here we implicitly assumed that dust-to-gas ratio is fairly constant throughout the Galaxy, which is reasonable as inferred from the well-known good correlation between total (i.e., HI plus H₂) hydrogen column density and color excess of extinction (Bohlin et al. 1978; Heithausen & Mebold 1989; Rachford et al. 2009). Finally we note that the original form of the Schmidt law ($\psi \propto \rho_{\text{gas}}^2$ where ρ_{gas} is spatial gas density) was proposed to explain the smaller vertical scale height of young stars than that of interstellar gas (Schmidt 1959; Fuchs et al. 2009).

In the case B2, we expect that the dust column density inferred from infrared SED fits, Σ_{dIR} , is constant around $\Sigma_{d,\text{crit}} \equiv 2\kappa_{d,\text{eff}}^{-1} = 0.96 [M_{\odot} \text{pc}^{-2}]$. This is checked by Fig. 22, where correlation between U_{TIR} and Σ_{dIR} is shown. As expected, the values of Σ_{dIR} do not show any trend against U_{TIR} , with the mean value close to $\Sigma_{d,\text{crit}}$. Many of galaxies having large deviations from $\Sigma_{d,\text{crit}}$ have large observational errors. Note that no galaxies are found in the region of $U_h < 0.1$ simply because the fit is limited by the minimum value $U_h = 0.1$ of the physical dust model.

We fit the $U_{\text{TIR}}-U_h$ relation by a linear ($U_h = 10^a U_{\text{TIR}}$) relation and the results are presented in Table 4 for the AKARI-SDSS and AKARI-HIPASS samples. Here we considered only the errors of $\log_{10} U_h$, because the errors of $\log_{10} L_{\text{TIR}}$ are much smaller, as mentioned in §3.2. The proportionality constant is different by just a factor of 1.5 for the two samples, indicating that our result is not seriously affected by the selection bias. We also tried a power-law ($U_h = 10^a U_{\text{TIR}}^b$) relation and a three-dimensional plane fit in the space of $\log_{10} R$, $\log_{10} L_{\text{TIR}}$, and $\log_{10} U_h$. The results are shown in Table 4, and these fits also indicate that the simple relation of $U_h \propto U_{\text{TIR}} \propto L_{\text{TIR}}/R^2$ is a good description of the observed correlation.

Table 4. Functional Fits to the $U_{\text{TIR}}-U_h$ Relation

	AKARI-SDSS	AKARI-HIPASS
Linear Fit*		
a	-0.097 ± 0.006	0.107 ± 0.005
$\sigma_{\text{lg}U}^{\text{obs}}$	0.354	0.344
$\sigma_{\text{lg}U}^{\text{int}}$	0.303	0.305
Power-law Fit†		
a	-0.085 ± 0.006	0.127 ± 0.006
b	0.934 ± 0.011	1.109 ± 0.012
$\sigma_{\text{lg}U}^{\text{obs}}$	0.352	0.350
$\sigma_{\text{lg}U}^{\text{int}}$	0.300	0.311
3D Plane Fit‡		
a	-7.566 ± 0.108	-10.341 ± 0.120
b	-2.179 ± 0.034	-1.850 ± 0.035
c	0.907 ± 0.011	1.168 ± 0.013
$\sigma_{\text{lg}U}^{\text{obs}}$	0.332	0.346
$\sigma_{\text{lg}U}^{\text{int}}$	0.277	0.307
$\langle \sigma_{\text{lg}U}^{\text{fit}} \rangle$	0.184	0.160

* $\log_{10} U_h = a + \log_{10} U_{\text{TIR}}$

† $\log_{10} U_h = a + b \log_{10} U_{\text{TIR}}$

‡ $\log_{10} U_h = a + b \log_{10}(R/\text{kpc}) + c \log_{10}(L_{\text{TIR}}/L_{\odot})$

We estimated the physical dispersion of U_h from the mean relation as follows. We define $\Delta_{\text{lg}U}^{\text{obs}}$ as the observed deviation of $\log_{10} U_h$ of each galaxy from the best-fit relations. Then the observed median of $|\Delta_{\text{lg}U}^{\text{obs}}|$ was converted into the observed standard deviation $\sigma_{\text{lg}U}^{\text{obs}}$ by using the Gaussian relation (median of $|x|$ is 0.674σ). The use of the median is to avoid the effect of a small number of outliers having large $|\Delta_{\text{lg}U}^{\text{obs}}|$. The quantity $\sigma_{\text{lg}U}^{\text{obs}}$ includes the observational errors of U_h in the SED fittings, and the intrinsic (i.e., physical) standard deviation $\sigma_{\text{lg}U}^{\text{int}}$ was calculated as

$$\sigma_{\text{lg}U}^{\text{int}} = [(\sigma_{\text{lg}U}^{\text{obs}})^2 - \langle \sigma_{\text{lg}U}^{\text{fit}} \rangle^2]^{\frac{1}{2}}, \quad (24)$$

where $\langle \sigma_{\text{lg}U}^{\text{fit}} \rangle$ is the mean of 1σ errors of $\log_{10} U_h$ in the SED fits. The results for $\sigma_{\text{lg}U}^{\text{obs}}$, $\sigma_{\text{lg}U}^{\text{int}}$ and $\langle \sigma_{\text{lg}U}^{\text{fit}} \rangle$ are shown in Table 4, and $\sigma_{\text{lg}U}^{\text{int}} \sim 0.3$ is indicated for all cases. This corresponds to $\sim 13\%$ dispersion in terms of the modified blackbody temperature, using $U_h \propto T_d^{4+\beta}$ and $\beta = 1.75$.

5.4. Dust Mass versus Metal Mass

If the interpretation of the case B2 distribution is correct for the observed $U_{\text{TIR}}-U_h$ correlation, this can further be tested by checking the trend about M_{dIR} against M_d , since the case B2 predicts the scaling of $M_{\text{dIR}}/M_d \sim (\tau_{d,\text{eff}}^{\text{tot}})^{-1} \propto \Sigma_d^{-1}$. For this purpose we need to measure the total dust amount in a galaxy independently of the infrared emission. Though it is difficult to directly measure M_d , the total metal mass of a galaxy in the gas phase, M_Z , is an indicator of M_d because grains are made from metals. For a part of the AKARI-SDSS sample, the gas-phase metallicity Z and M_{HI} measurements are available, and we can estimate the HI-gas-phase metal mass as

$$M_{Z(\text{HI})} \equiv 1.36 Z M_{\text{HI}} = 1.36 Z f_{\text{HI}} M_{\text{H}} = f_{\text{HI}} M_Z, \quad (25)$$

where f_{HI} is the HI fraction of the total hydrogen gas mass, M_{H} . [The numerical factor corrects the hydrogen

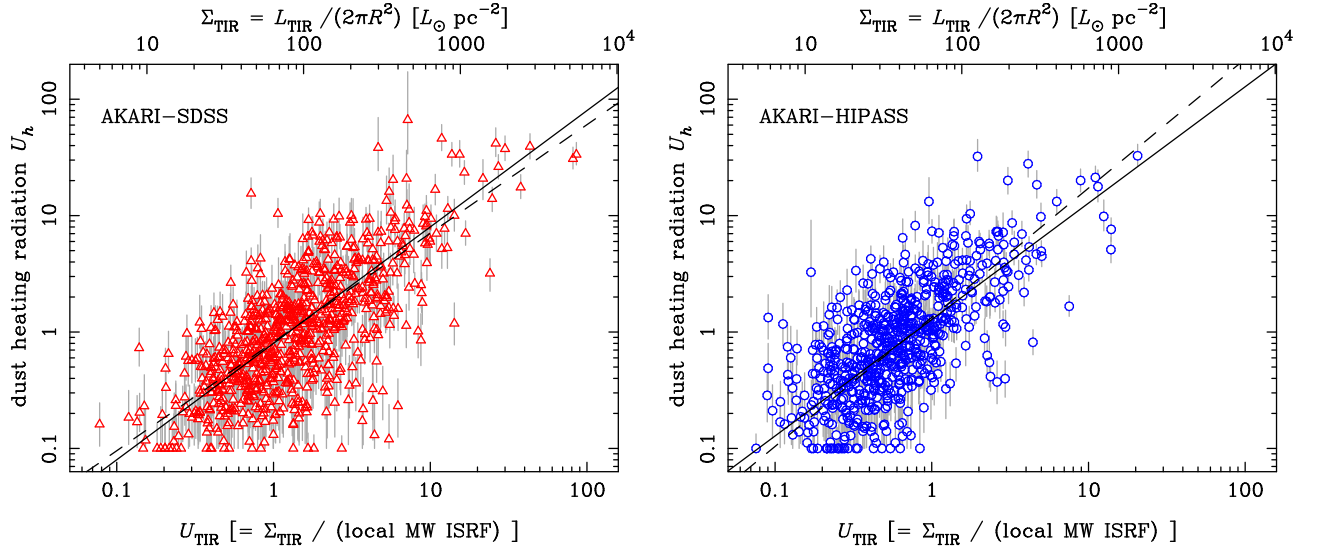


Fig. 21. Dust-heating radiation field strength (U_h , estimated by infrared SED fittings) versus global infrared radiation field strength [$\Sigma_{\text{TIR}} = L_{\text{TIR}}/(2\pi R^2)$], for the AKARI-SDSS (left) and AKARI-HIPASS (right) samples. The parameter U_{TIR} is Σ_{TIR} normalized by the bolometric strength of the local (solar neighborhood) ISRF in the Milky Way, which can directly be compared with U_h . The solid and dashed lines are the best-fit linear ($U_h \propto U_{\text{TIR}}$) and power-law ($U_h \propto U_{\text{TIR}}^b$) relations, respectively.

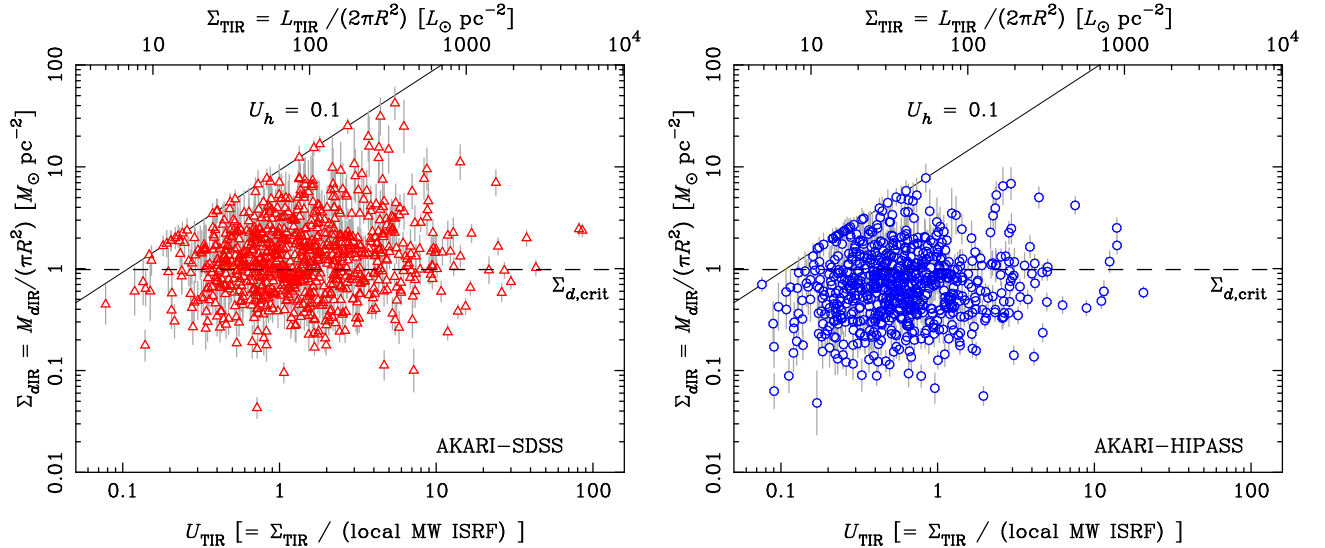


Fig. 22. Column density of heated dust Σ_{dIR} versus global infrared radiation field strength (U_{TIR} or Σ_{TIR} for the bottom or top ordinate), for the AKARI-SDSS (left) and AKARI-HIPASS (right) samples. The critical dust column density, $\Sigma_{\text{d,crit}} = 0.98 M_{\odot} \text{pc}^{-2}$ corresponding to the effective dust optical depth $\tau_{\text{d,eff}}^{\text{tot}} = 1$, is indicated by the dashed line. The solid line shows the locations when $U_h = 0.1$, and there is no galaxies in the upper-left region because the physical dust model is limited to $U_h \geq 0.1$. The errors are from those for M_{dIR} .

mass fraction of the total baryon, $X = 0.74$ (Grevesse et al. 2010).] Some of the AKARI-SDSS galaxies and all of the AKARI-HIPASS galaxies have M_{HI} measurements but no metallicity measurements. To calculate $M_{Z(\text{HI})}$ for these galaxies, we adopt a mean value of $Z_{\text{av}} = 0.05$ as inferred from the mass-metallicity plot of the AKARI-SDSS galaxies (Fig. 8). This metallicity is higher than the solar abundance, but not unreasonable for dusty galaxies selected by AKARI, taking also into account the systematic uncertainties in the metallicity measurements (see footnote 2).

Then the total dust mass $M_d = f_{dZ} M_Z$ is related to $M_{Z(\text{HI})}$ as

$$M_d = f_{dZ} f_{\text{HI}}^{-1} M_{Z(\text{HI})}, \quad (26)$$

using the dust fraction f_{dZ} of the total metal mass in interstellar gas. Observations of interstellar medium in our Galaxy suggest $M_d/M_H \sim 0.0073$, corresponding to $f_{dZ} \sim 0.3$ (Draine et al. 2007). Although f_{HI} is unknown for our samples, we expect $M_d/M_{Z(\text{HI})} \sim 1$ for galaxies with f_{HI} of order unity.

Figure 23 plots M_{dIR} against $M_{Z(\text{HI})}$ for the two samples. It can be seen that many galaxies are located at the region of $M_{\text{dIR}} < M_{Z(\text{HI})}$, and a clear boundary can be seen at $M_{\text{dIR}} \sim M_{Z(\text{HI})}$, as expected. There are a small number of AKARI-SDSS galaxies showing high $M_{\text{dIR}}/M_{Z(\text{HI})}$, but most of them are galaxies without metallicity estimates and plotted using Z_{av} . Most galaxies with metallicity measurements have $M_{\text{dIR}} \lesssim M_{Z(\text{HI})}$.

There are galaxies showing $M_{\text{dIR}}/M_{Z(\text{HI})} \ll 1$, and the origin of this small value is interesting. A possibility is that the dust production efficiency from metals is low, i.e., $M_d \ll M_{Z(\text{HI})}$. There are observational indications that low-metallicity dwarf galaxies have lower dust-to-metal ratios than giant galaxies (Galliano et al. 2003, 2005; Hunt et al. 2005; but see also James et al. 2002). Draine et al. (2007) also found that dust-to-metal ratio is lower for low-metallicity galaxies having $A_{\text{O}} \lesssim 8.1$, but they argued that infrared emission from such galaxies is from a small region compared with the whole galaxy, and the dust-to-metal ratio becomes consistent with the MW value if it is calculated using gas mass and metallicity in the regions of infrared emission. In any case, galaxies in our sample have $A_{\text{O}} \gg 8.1$ as we showed in Fig. 8, and hence the low metallicity effect is unlikely to be the origin of the small $M_{\text{dIR}}/M_{Z(\text{HI})}$ values in our sample. Indeed, we plot $M_{\text{dIR}}/M_{Z(\text{HI})}$ versus metallicity for the AKARI-SDSS galaxies with available metallicity measurements in Fig. 24, and there is no systematic trend.

Instead we argue that the dispersion in $M_{\text{dIR}}/M_{Z(\text{HI})}$ originates from the difference between M_{dIR} and M_d . The good correlation between U_{TIR} and U_h indicates the case B2 distribution where only a part of dust is radiated by heating sources. In this case we expect $M_{\text{dIR}}/M_d \propto \Sigma_d^{-1}$, and hence $M_{\text{dIR}}/M_{Z(\text{HI})} \propto \Sigma_{Z(\text{HI})}^{-1}$ if $f_{dZ} f_{\text{HI}}^{-1}$ is constant for all galaxies, where $\Sigma_{Z(\text{HI})} \equiv M_{Z(\text{HI})}/(\pi R^2)$. Figure 25 shows this correlation, and the data of both samples clearly show the expected correlation. This pro-

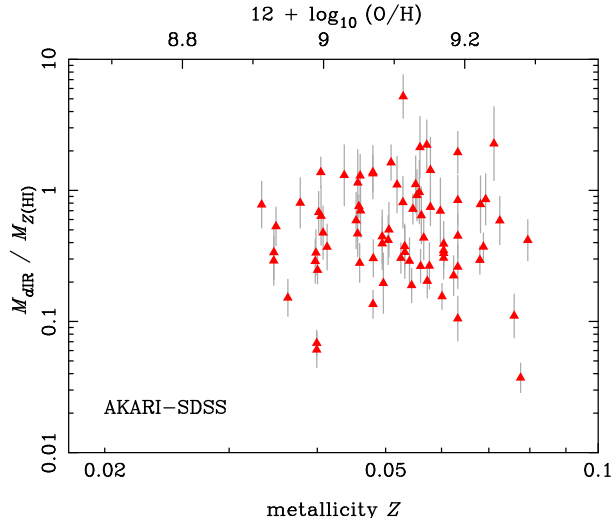


Fig. 24. The ratio of $M_{\text{dIR}}/M_{Z(\text{HI})}$ versus metallicity for the AKARI-SDSS galaxies with available Z and M_{HI} measurements. The errors are from those for M_{dIR} .

vides a further support to the interpretation of $U_{\text{TIR}}-U_h$ relation by the distribution case B2. Given the constant nature of Σ_{dIR} found in Fig. 22, the correlation $M_{\text{dIR}}/M_{Z(\text{HI})} = \Sigma_{\text{dIR}}/\Sigma_{Z(\text{HI})} \propto \Sigma_{Z(\text{HI})}^{-1}$ may seem rather trivial, but this figure demonstrates that Σ_{dIR} stays constant even if $\Sigma_{Z(\text{HI})}$ significantly changes. According to this interpretation, we expect $M_{\text{dIR}}/M_d \sim 1$ when $\tau_{d,\text{eff}}^{\text{tot}} \sim 1$, i.e., $\Sigma_d \sim \Sigma_{d,\text{crit}} = 0.98 M_{\odot} \text{pc}^{-2}$. The data is consistent with this expectation for a reasonable value of $f_{dZ} f_{\text{HI}}^{-1} \sim 1$ ($\Sigma_{Z(\text{HI})} \sim \Sigma_d$).

Finally let us examine the assumption of $f_{dZ} f_{\text{HI}}^{-1}$ being a constant. The assumption of constant f_{dZ} is theoretically reasonable if the dust production process works similarly in all galaxies. It is also known that the dust-to-gas ratio estimated by extinction in optical bands for nearby galaxies and quasar absorption line systems (QALSs) is correlated well with metallicity, indicating that M_d/M_Z is roughly constant (Issa et al. 1990; Boissier et al. 2004; Vladilo et al. 2006). It should be noted that the extinction in QALSs is sensitive to all dust grains in a system on the line of sight, in contrast to M_{dIR} that traces only dust heated by radiation. The variation of f_{HI} in different galaxies may also lead to the scaling of $M_{\text{dIR}}/M_{Z(\text{HI})} \propto \Sigma_{Z(\text{HI})}^{-1}$. However, if this effect is significant, we expect that the sequence will appear in the region of $M_{\text{dIR}}/M_{Z(\text{HI})} \gtrsim 1$ because $f_{\text{HI}} < 1$, which is opposite to the observed trend.

5.5. Extension to Circumnuclear Starbursts

We have seen that the infrared emission from the AKARI-SDSS and AKARI-HIPASS galaxies are described well by the case B2 of dust distribution. However, the dynamic range of U_{TIR} is limited to $0.1 \lesssim U_{\text{TIR}} \lesssim 100$, and here we examine the AKARI-SB sample to extend this range.

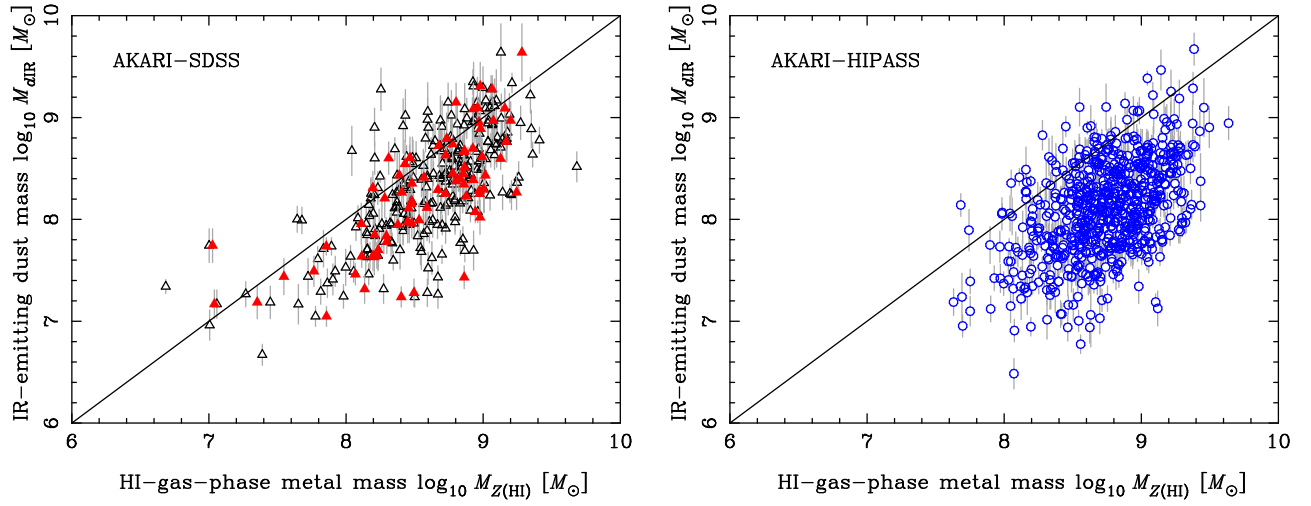


Fig. 23. Heated dust mass M_{dIR} versus HI-gas-phase metal mass $M_{Z(HI)}$ for the AKARI-SDSS (left) and AKARI-HIPASS (right) samples. For red filled triangles in the left panel, $M_{Z(HI)}$ is calculated using metallicity estimates for each galaxy, while that of open symbols is calculated using a mean metallicity of $Z_{av} = 0.05$ because metallicity measurements are not available.

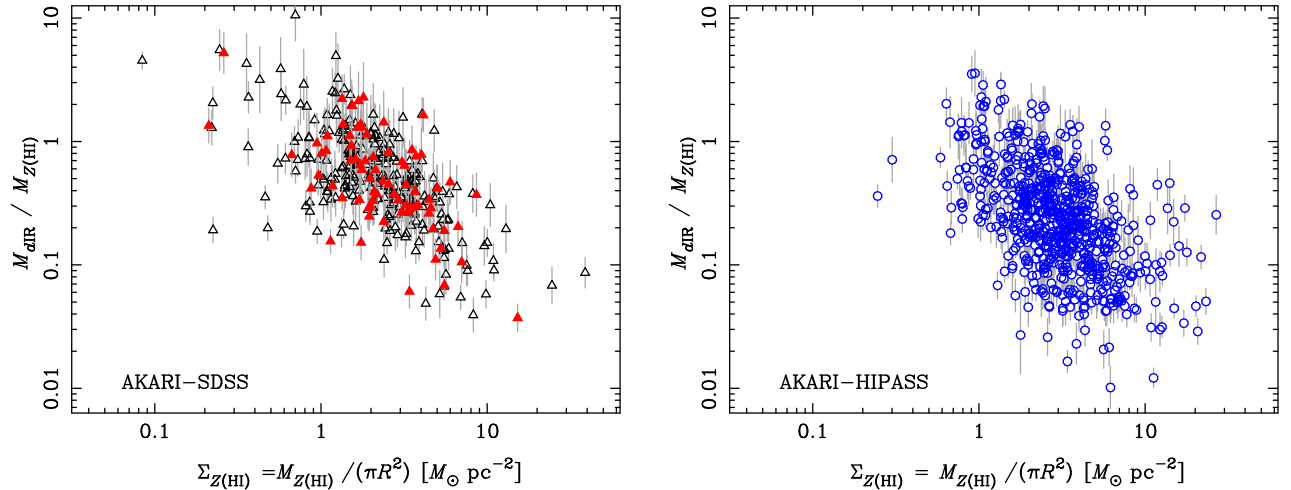


Fig. 25. The ratio of $M_{dIR}/M_{Z(HI)}$ versus column density of HI-gas-phase metal $\Sigma_{Z(HI)}$ for the AKARI-SDSS (left) and AKARI-HIPASS (right) samples. Different symbols have the same meanings as those in Fig. 23. The errors are from those for M_{dIR} .

Figure 26 shows the $L_{\text{TIR}}-U_h$, $U_{\text{TIR}}-U_h$, and $U_{\text{TIR}}-\Sigma_{\text{dIR}}$ relations of the AKARI-SB galaxies in comparison with the AKARI-SDSS sample. The AKARI-SB galaxies are distributed at similar locations to the AKARI-SDSS galaxies in the $L_{\text{TIR}}-U_h$ plane, but they have much larger U_{TIR} . An interesting trend is found for U_h against U_{TIR} ; it is roughly constant and there seems an upper bound of $U_{h,\text{max}} \sim 50$, which is in sharp contrast to the AKARI-SDSS galaxies showing a tight correlation of $U_h \propto U_{\text{TIR}}$. But these two data sets are not inconsistent with each other. The dispersion of the U_h/U_{TIR} ratio for the AKARI-SDSS galaxies becomes larger at $U_h \gtrsim 10$, and the distribution of the AKARI-SDSS galaxies is smoothly connected to that of the AKARI-SB sample. Corresponding to the constant nature of U_h against U_{TIR} , Σ_{dIR} is roughly proportional to U_{TIR} , as expected from eq. (18).

A remarkable result is obtained by comparison between M_{dIR} and H_2 mass estimated from CO observations, M_{H_2} , for the AKARI-SB sample. These two independently measured quantities are correlated much better, as shown in the histogram of $M_{\text{dIR}}/M_{\text{H}_2}$ in Fig. 26, than the $M_{\text{dIR}}-M_{\text{HI}}$ correlation of the AKARI-SDSS galaxies. The majority of galaxies are clustering around $M_{\text{dIR}}/M_{\text{H}_2} \sim 0.015$ within a factor of 2, and the ratio of 0.015 is close to the expectation of typical dust-to-hydrogen ratio $f_{\text{dH}} = 1.36 f_{\text{dZ}} Z$. It is known that molecular hydrogen is the dominant form of hydrogen when the gas column density is very high like circumnuclear starbursts (Kennicutt 1998; Bigiel et al. 2008). Therefore, this result implies that the infrared-emitting dust mass is close to the total dust mass, i.e., $M_{\text{dIR}} \sim M_{\text{d}}$.

We consider that this result can be interpreted as follows. As argued by Kennicutt (1998), L_{TIR} can be regarded as a good SFR indicator for the K98 SB sample. Using the relations of $M_{\text{dIR}} \sim 0.015 M_{\text{H}_2}$ and $L_{\text{TIR}} \propto M_{\text{dIR}} U_h$, U_h is equivalent to the star formation efficiency (SFE), ψ_e , which is defined as SFR per unit hydrogen gas mass. Using eq. (4) and (16), we find

$$\psi_e \equiv \frac{\psi}{M_{\text{H}}} = 0.24 U_h [\text{Gyr}^{-1}], \quad (27)$$

and the upper limit of $U_{h,\text{max}} \sim 50$ is translated into the upper limit of $\psi_{e,\text{max}} \sim 10 \text{ Gyr}^{-1}$. Then, the systematic change of the $U_{\text{TIR}}-U_h$ relation can be explained if there is a fundamental upper limit on SFE by the physics of star formation (see §6.2 for more discussion on the origin of this upper limit).

If this upper limit exists, the distribution case B2 is not allowed when $U_{\text{TIR}} > U_{h,\text{max}}$. For the case B2, star formation must occur within a thin layer of the disk whose dust column density is $\Sigma_{\text{d}} \sim \Sigma_{\text{d,crit}}$ (or $\Sigma_{\text{H}} \sim \Sigma_{\text{H,crit}} \sim 10^2 M_{\odot} \text{ pc}^{-2}$, adopting a typical dust-to-hydrogen ratio). Then there is a maximum of the surface SFR density [$\Sigma_{\text{SFR}} \equiv \psi/(\pi R^2)$] for the case B2 determined by $\psi_{e,\text{max}}$ and $\Sigma_{\text{H,crit}}$, corresponding to $U_{\text{TIR}} \sim U_{h,\text{max}}$. When Σ_{SFR} is higher than this, the gas column density of the star forming layer must proportionally increase beyond $\Sigma_{\text{H,crit}}$ because of the limit of $\psi_{e,\text{max}}$, and hence

$\Sigma_{\text{dIR}} \propto \Sigma_{\text{SFR}} \propto U_{\text{TIR}}$ while U_h becomes constant at $U_{h,\text{max}}$. This situation corresponds to the case B1 rather than B2, and the transition from B2 occurs around $U_{\text{TIR}} \sim U_{h,\text{max}}$.

This result should have some implications for the well-known Kennicutt-Schmidt law on the plane of $\Sigma_{\text{H}}-\Sigma_{\text{SFR}}$. We will discuss about this issue in more detail in §6.2.

6. Discussion

6.1. Paucity of Optically Thin Galaxies and Radiative Feedback?

We have found that galaxies studied here are well described by the distribution case B1 or B2, meaning that they are optically thick to dust-heating radiation on a galactic scale ($\tau_{\text{d,eff}}^{\text{tot}} \gtrsim 1$). This is consistent with the distribution of the infrared-to-optical luminosity ratio (Fig. 16); the distribution extends down to $L_{\text{TIR}}/L_r \sim 1$ with a sudden drop of the galaxy number at $L_{\text{TIR}}/L_r < 1$, indicating a paucity of optically thin galaxies ($\tau_{\text{d,eff}}^{\text{tot}} \lesssim 1$). This is also indicated by the sequence of $M_{\text{dIR}}/M_{\text{Z(HI)}} \propto \Sigma_{\text{Z(HI)}}^{-1}$ in Fig. 25. If there are a significant number of optically thin galaxies, such galaxies should appear in the region of $\Sigma_{\text{Z(HI)}} \lesssim 1 M_{\odot} \text{ pc}^{-2}$ with a constant value of $M_{\text{dIR}}/M_{\text{Z(HI)}} \sim 1$, corresponding to $\Sigma_{\text{d}} \lesssim \Sigma_{\text{d,crit}}$ and $M_{\text{dIR}}/M_{\text{d}} \sim 1$. However, such galaxies are not found, and the sequence seems to stop at $\Sigma_{\text{d}} \sim \Sigma_{\text{d,crit}}$ ($\tau_{\text{d,eff}}^{\text{tot}} \sim 1$).

If the optical thickness to dust-heating radiation does not have any effect on galaxy formation efficiency, a fine-tuning would be required for the sharp drop of galaxy distribution around $\tau_{\text{d,eff}}^{\text{tot}} \sim 1$. A possible explanation is a selection effect; optically thin galaxies would have small infrared-to-optical luminosity ratio and hence could be missed in the samples selected by infrared emission. To check this possibility, we plot in Fig. 27 velocity-integrated 21-cm flux density (S_{int}) versus angular size (θ_{P90}) for the SDSS-HI and HIPASS samples, in comparison with the AKARI-SDSS and AKARI-HIPASS galaxies. The lines corresponding to several values of HI column density $\Sigma_{\text{HI}} \equiv M_{\text{HI}}/(\pi R^2)$ are also depicted. It can be seen that there is no significant difference between the distributions of Σ_{HI} for the AKARI-detected and -nondetected galaxies, and the paucity of galaxies in the region of $\Sigma_{\text{HI}} \lesssim 10 M_{\odot} \text{ pc}^{-2}$ can be seen, roughly corresponding to $\tau_{\text{d,eff}}^{\text{tot}} \lesssim 1$ for typical values of f_{HI} , f_{dZ} , and Z . Hence the infrared selection bias cannot explain the paucity of optically thin galaxies. It should be noted that the beam size of HIPASS is 15.5 arcmin, which is much larger than the galaxy sizes, and hence there should be no selection bias about surface brightness in the HI data.

Therefore we consider that there is a physical effect reducing the efficiency of galaxy formation when $\tau_{\text{d,eff}}^{\text{tot}} \lesssim 1$. Because the opacity is to dust-heating radiation, it is most likely the radiative feedback by the dust photoelectric heating of ISM. A part (typically $\epsilon_{\text{PE}} \sim 1-10\%$) of radiation energy absorbed by dust grains is converted to photoelectrons and subsequently heat ISM, and this effect is large enough to be the dominant heating process in many phases of ISM in galaxies (see, e.g., Bakes &

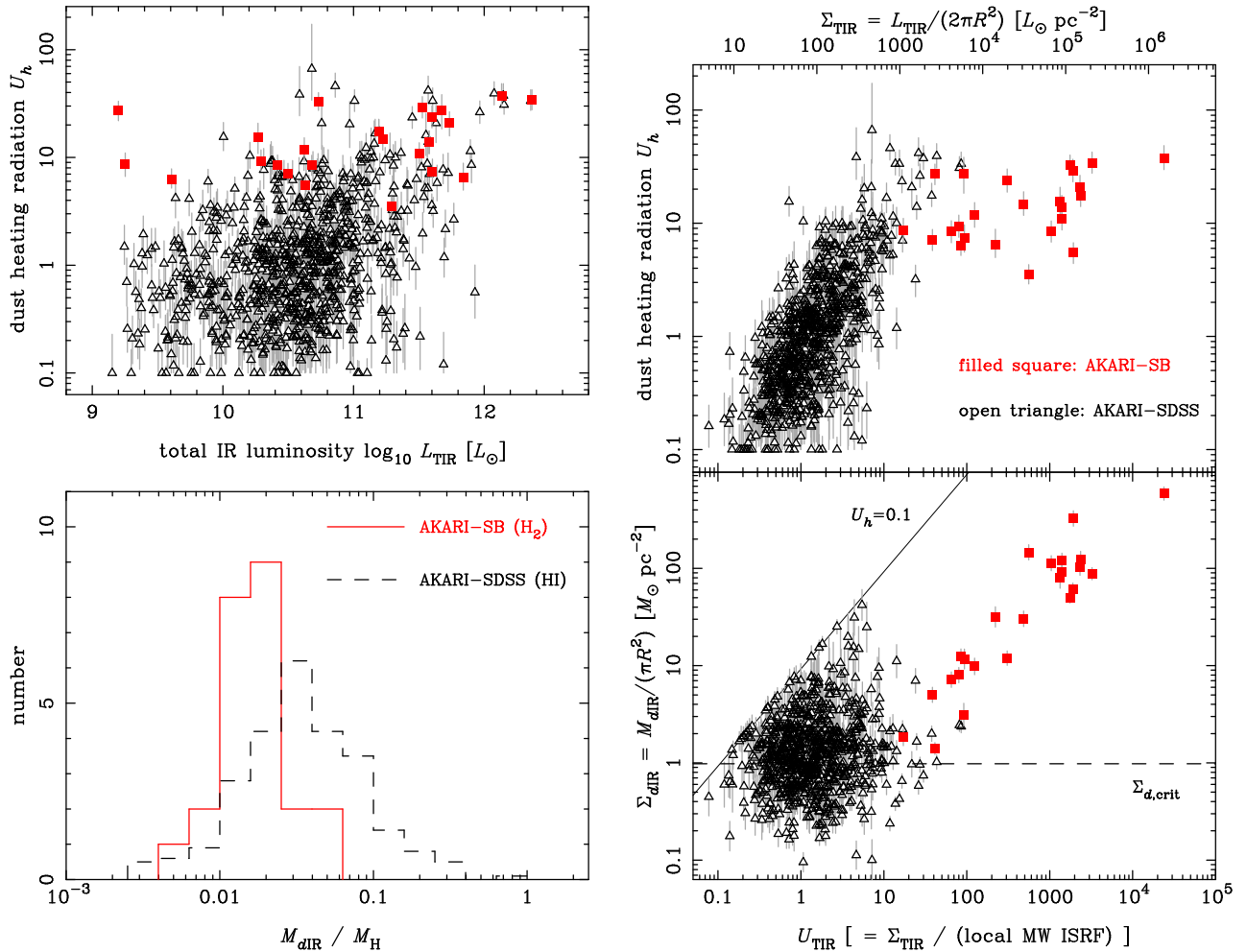


Fig. 26. The properties of galaxies in the AKARI-SB sample. The upper-left, upper-right, and lower-right panels are the same as Figs. 18, 21, and 22, respectively, but showing the AKARI-SB galaxies by the filled red squares, in comparison with the AKARI-SDSS sample (open triangles). The lower-left panel shows the histogram of the mass ratio of heated dust to hydrogen gas, $M_{\text{dIR}}/M_{\text{H}}$, where M_{H} is H_2 and H I mass for the AKARI-SB and AKARI-SDSS samples, respectively. The histogram of the AKARI-SDSS sample is multiplied by a factor of 0.1 for comparison.

Tielens 1994; Wolfire et al. 1995; Rubin et al. 2009). Then, in $\tau_{\text{d,eff}}^{\text{tot}} \lesssim 1$ galaxies, it is expected that the lack of self-shielding of dust-heating radiation leads to the suppression of star formation activity and reduction of neutral gas in ISM on a galactic scale. Bigiel et al. (2010) found that star formation efficiency becomes extremely low with decreasing Σ_{HI} in outer disk of nearby galaxies, which is consistent with the picture discussed here.

On the other hand, in the large limit of Σ_{HI} , Fig. 27 shows the paucity of galaxies at the region of $\Sigma_{\text{HI}} \gtrsim 10^2 M_{\odot} \text{pc}^{-2}$. This is likely because most of gas tends to be molecular when gas column density is high, resulting in a saturation of Σ_{HI} , as observed for nearby galaxies (Bigiel et al. 2008). The efficient self-shielding of dust-heating radiation may be responsible for converting H I into H_2 . The lack of both large and small Σ_{HI} galaxies by these effects may explain the known good correlation between H I mass and size, $M_{\text{HI}} \propto R^2$ (Haynes & Giovanelli 1984; Rosenberg & Schneider 2003; Garcia-Appadoo et al. 2009; van der Kruit & Freeman 2011). The dispersion in

M_{HI}/R^2 seems especially small when H I size is used for R (Rosenberg & Schneider 2003), further indicating that $\tau_{\text{d,eff}}^{\text{tot}}$ is playing an essential role.

6.2. Implications for the Kennicutt-Schmidt Relation

The quantities about infrared emission discussed in this work are mostly in surface densities of galaxies, e.g., U_{TIR} or Σ_{dIR} . These quantities are closely related to the surface density of SFR, Σ_{SFR} , and surface hydrogen gas density, Σ_{H} . Since the correlation between Σ_{SFR} and Σ_{H} is frequently discussed in the literature as the Kennicutt-Schmidt relation (Schmidt 1959; Kennicutt 1998), it is interesting to discuss about it in light of the results obtained in this work.

In Figure 28 we show the $\Sigma_{\text{SFR}}-\Sigma_{\text{H}}$ plot for the AKARI-SDSS and SDSS- H I samples, using H I gas mass for Σ_{H} . For the K98 SB sample, we plot the original data for the 36 galaxies in K98 (Σ_{H} from H_2 mass by CO observations), corrected only for SFR into the Kroupa IMF. The SFRs of the SDSS galaxies are from optical spectra, while

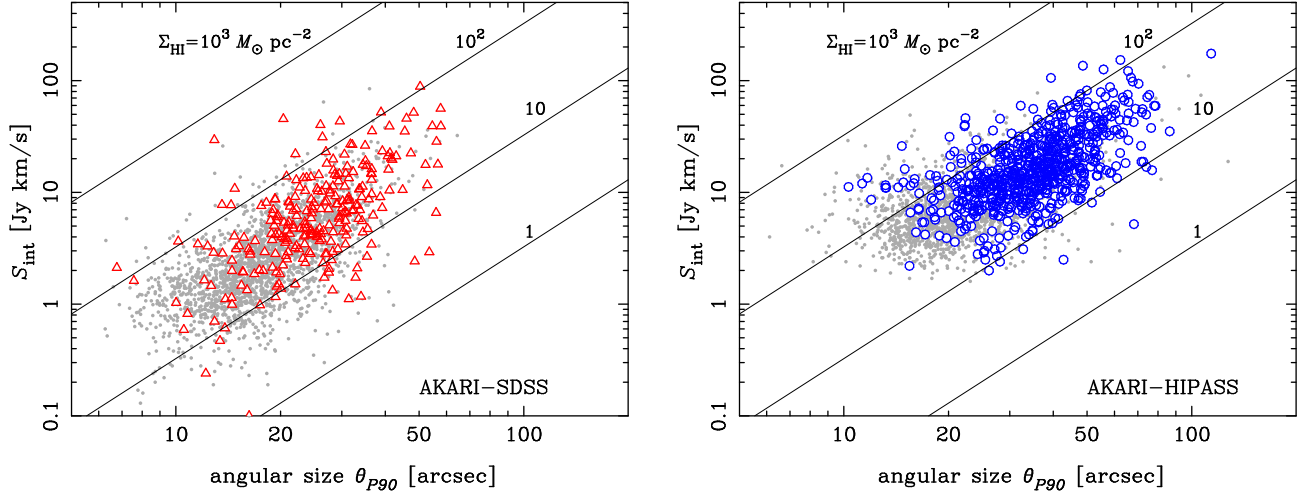


Fig. 27. Velocity-integrated flux density of the 21-cm emission (S_{int}) versus angular size (θ_{P90}), for the AKARI-SDSS (left) and AKARI-HIPASS (right) samples. The grey dots are for galaxies whose infrared emission was not detected by AKARI. The solid lines correspond to several values of H I column density Σ_{HI} as indicated in the panels ($S_{\text{int}} \propto M_{\text{HI}}/d_L^2$, $\theta_{P90} = R/d_A$, and hence $\Sigma_{\text{HI}} \propto S_{\text{int}}/\theta_{P90}^2$). For these solid lines we assumed a redshift $z = 0.02$ that is typical for the samples here, though the dependence on z is very small only by the cosmological effect proportional to $(1+z)$.

those of the K98 SB sample are from L_{TIR} . There is no good correlation between Σ_{SFR} and Σ_{HI} for galaxies in the SDSS-based samples at $\Sigma_{\text{H}} \lesssim 100 M_{\odot} \text{pc}^{-2}$, which is consistent with the results of K98 for normal spirals and of Bigiel et al. (2008) for sub-kpc regions of nearby galaxies. This range of Σ_{H} roughly corresponds to $\tau_{d,\text{eff}}^{\text{tot}} \lesssim 1$, and as argued in §6.1, the radiative feedback process seems to be working to suppress the star formation activity. Then the relation between SFR and H I gas amount would become complicated by unstable competition between star formation and its feedback. This may give an explanation for the large dispersion in the $\Sigma_{\text{SFR}}\text{-}\Sigma_{\text{HI}}$ relation.

On the other hand, we have found in §5.5 that U_h is constant at $U_h \sim 50$ for the AKARI-SB sample, corresponding to a constant SFE of $\psi_{e,\text{max}} \sim 10 \text{ Gyr}^{-1}$, i.e., $\Sigma_{\text{SFR}} \propto \Sigma_{\text{H}}$. This SFE is equivalent to the star formation time scale of $t_{\text{SF},\text{min}} \equiv \psi_{e,\text{max}}^{-1} \sim 0.1 \text{ Gyr}$. It is interesting to note that this characteristic SFE is in nice agreement with those found in the correlation between M_{H_2} and SFR for a wide variety of galaxies as well as molecular clouds in the Galaxy (Gao & Solomon 2004; Wu et al. 2005; Bigiel et al. 2008; Evans et al. 2009), when the gas mass is measured from tracers of dense molecular gas. These results indicate that $\psi_{e,\text{max}}$ is a universal characteristic value originating from the physics of star formation in ISM, rather than time scales on a galactic scale. It is widely known that the efficiency of star formation from molecular clouds is typically a few percent in mass fraction, and typical dynamical time scales of molecular clouds are Myr, resulting in a star formation time scale of $\sim 0.1 \text{ Gyr}$. This maximum SFE $\psi_{e,\text{max}}$ seems to be achieved on a galactic scale when $\tau_{d,\text{eff}}^{\text{tot}} \gg 1$ ($\Sigma_{\text{H}} \gg 100 M_{\odot} \text{pc}^{-2}$) because the self-shielding effect of dust-heating radiation is working for efficient gas cooling. Most of interstellar gas would be molecular in such galaxies.

Now we may interpret the overall trend of the galaxy

distribution on the $\Sigma_{\text{SFR}}\text{-}\Sigma_{\text{H}}$ plane by the strong dependence of SFE on the dust opacity, as follows. There are very few galaxies having $\tau_{d,\text{eff}}^{\text{tot}} \ll 1$, because the feedback suppresses an efficient star formation. Galaxies appear in the region of $\tau_{d,\text{eff}}^{\text{tot}} \gtrsim 1$ with a large dispersion in the Kennicutt-Schmidt law, because SFE rapidly increases around $\tau_{d,\text{eff}}^{\text{tot}} \sim 1$. Then SFE continues to increase and asymptotically reaches the maximum value of $\psi_{e,\text{max}} \sim 10 \text{ Gyr}^{-1}$ at $\tau_{d,\text{eff}}^{\text{tot}} \gg 1$. We expect many galaxies around $\tau_{d,\text{eff}}^{\text{tot}} \sim 1$ because star formation time scale is relatively longer than that in more dusty galaxies.

6.3. Implications for Theoretical Modelings of Galaxy Formation

There are a few implications of the results obtained by this work for theoretical modeling of galaxy formation and evolution. First of all, the tight correlation between U_h and U_{TIR} for normal galaxies provides a convenient way to calculate infrared SEDs in cosmological galaxy formation models, in which the total dust-unabsorbed luminosity of stellar emission and size of a galaxy can be calculated in a relatively straightforward manner. When galaxies are optically thick in terms of $\tau_{d,\text{eff}}^{\text{tot}}$ as indicated by our study, the total stellar luminosity gives a direct estimate of L_{TIR} . Then U_h or T_d can easily be calculated from the $U_{\text{TIR}}\text{-}U_h$ relation, which is more reliable than $L_{\text{TIR}}\text{-}T_d$ relation because of the tighter correlation and more solid physical background. There is no particular reason to expect that this relation does not hold for high redshift galaxies, if the dust properties are not significantly different and the spatial distribution of stars and dust grains is the case B2. It must be examined whether the existing *ab initio* galaxy formation models of infrared emission satisfy this relation, especially at $z \sim 0$.

Another important implication is the strong depen-

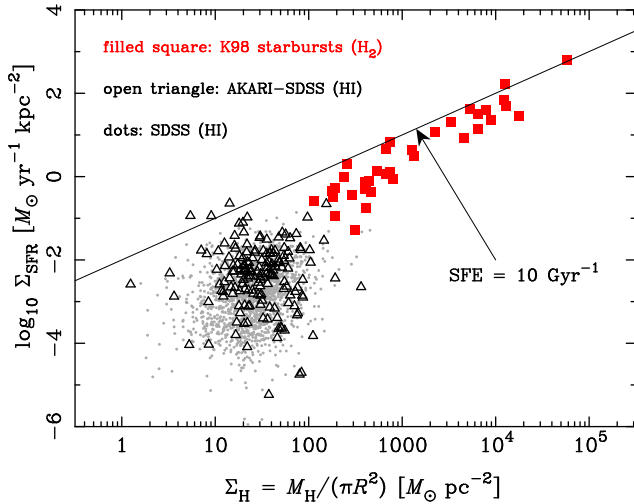


Fig. 28. SFR column density versus hydrogen gas column density (the Kennicutt-Schmidt law). The red squares are for the circumnuclear starbursts of the K98 sample, estimating gas mass from H_2 and SFR from L_{TIR} . The AKARI-SDSS galaxies are plotted by triangles, and grey dots are for SDSS galaxies without AKARI detection, estimating gas mass from HI and SFR from SDSS spectra. The relation corresponding to star formation efficiency (SFE) $\psi_e = 10 \text{ Gyr}^{-1}$ is shown by the solid line.

dence of star forming activity on dust opacity or gas column density suggested in §6.1 and §6.2. Various feedback processes have intensively been discussed in the context of cosmological galaxy formation (e.g., Benson et al. 2003; Baugh 2006; Silk 2011), but these feedback processes are not physically connected to the galaxy-scale dust opacity, $\tau_{d,\text{eff}}^{\text{tot}}$. Photoionization of hydrogens may have a similar dependence on gas column density, but it has a much larger opacity than $\tau_{d,\text{eff}}^{\text{tot}}$ by a factor of $\sim 3 \times 10^4$ for $M_d/M_H = 0.01$. Supernova/AGN feedbacks are unlikely related to the galaxy-scale dust opacity.

We have argued in §6.1 that the dust photoelectric heating of ISM is the likely process responsible for the feedback working in $\tau_{d,\text{eff}}^{\text{tot}} \lesssim 1$ galaxies. Using eq. (4), $1 M_\odot$ of star formation produces $3.2 \times 10^{49} (\epsilon_{PE}/0.03)$ erg by photoelectric heating, when most of heating radiation energy is absorbed into dust grains. This heating energy is comparable with and may even be larger than 1.1×10^{49} erg produced by the supernova feedback (assuming 10^{51} erg per one supernova, $8 M_\odot$ threshold for supernova explosions, and the Kroupa IMF). In contrast to supernova feedback, which is a local energy input only to dynamically connected regions, photoelectric heating could suppress star formation on the global scale in a galaxy when $\tau_{d,\text{eff}}^{\text{tot}} \lesssim 1$.

Such a feedback effect as a function of dust opacity (or gas column density) may systematically change the galaxy formation and evolution. Cosmological objects with dark matter mass M_{DM} virializing at redshift z have virial density proportional to $\rho_{\text{vir}} \propto (1+z)^3$, and the available baryon mass and galaxy size roughly scale with dark matter mass and virial radius, respectively. Therefore we expect that gas column density scales as $\propto M_{DM}^{1/3} (1+z)^2$,

indicating that this effect will accelerate star formation at higher redshifts, also weakly favoring star formation in massive objects at a fixed redshift.

This may have interesting implications for some major problems in the hierarchical galaxy formation scenario (e.g., Baugh 2006; Silk 2011). One is the difficulty to reproduce the early appearance of massive and quiescent galaxies at high redshifts (Cimatti et al. 2004; Glazebrook et al. 2004), and another is that the theory predicts too large stellar mass in massive dark halos ($\gtrsim 10^{12} M_\odot$) at $z \sim 0$ compared with the observed galaxy luminosity function (the so-called ‘‘overcooling’’ problem). If SFE is a strong function of $\tau_{d,\text{eff}}^{\text{tot}}$, it would increase the star formation activity at high-redshift compact dark halos. Massive objects have larger gas column density at a fixed redshift, which may be relevant to reproduce the well-known trend of downsizing in galaxy formation. On the other hand, dark halos collapsing at low redshifts are massive but have low densities, and star formation would be suppressed to alleviate the overcooling problem.

6.4. Comparison with Previous Studies

One of the most important results of this paper is the tight correlation between the dust-heating radiation strength U_h and the galaxy-scale infrared radiation strength U_{TIR} . The parameter U_{TIR} is equivalent to the infrared surface brightness, and the correlation of this quantity to infrared SED has been studied by Lehnert & Heckman (1996, hereafter LH96) and Chanial et al. (2007, hereafter C07).

LH96 estimated the size of 32 nearby starburst galaxies by $H\alpha$ images, and found a correlation between $L_{TIR}/(\pi R_{H\alpha})^2$ and infrared color temperature estimated by $60/100 \mu\text{m}$ flux ratios. They argued that a surrounding dust screen radiated by a radiation field strength of $L_{TIR}/(\pi R_{H\alpha})^2$ is an adequate zeroth-order description of their data, which is equivalent to our interpretation of the case B2 for normal star-forming galaxies. However, we also found that U_h becomes roughly constant for circumnuclear starbursts in the high SFR density region. The LH96 galaxies are in the range of $10^3 \lesssim L_{TIR}/(\pi R_{H\alpha}^2) \lesssim 10^5 L_\odot \text{ pc}^{-2}$, roughly corresponding to $10 \lesssim U_{TIR} \lesssim 10^3$ assuming that the $H\alpha$ radius is not different from the r -band radius used here. This is the region of transition from $U_h \propto U_{TIR}$ to a constant U_h , and indeed, the distribution of the LH96 galaxies is flatter than expected from the simple surrounding screen in the $S_{60\mu\text{m}}/S_{100\mu\text{m}}$ versus $L_{TIR}/(\pi R_{H\alpha}^2)$ plane (see their Fig. 5). Our result is thus not inconsistent with that of LH96, but revealed the correlation more quantitatively by larger statistics, using not only starbursts but also normal galaxies.

C07 studied on samples (~ 400 galaxies in total) including non-starburst galaxies. They estimated galaxy sizes by radio continuum (RC) images, and found a correlation of $\Sigma_{TIR} = L_{TIR}/(2\pi R_{RC}^2) \propto T_d^\delta$ with $\delta \sim 18.5$, where T_d is the dust temperature estimated by assuming the modified blackbody spectrum. The range of Σ_{TIR} is $\sim 10^1\text{--}10^5 L_\odot \text{ pc}^{-2}$ ($U_{TIR} \sim 0.1\text{--}10^3$). In contrast to LH96, they concluded that the surrounding dust screen

is ruled out because the observed slope of the correlation is significantly different from the expectation ($\delta = 4 + \beta$). Instead, they proposed another interpretation based on the Kennicutt-Schmidt law. Assuming a constant dust-to-gas ratio ($\Sigma_{\text{dIR}} \propto \Sigma_{\text{gas}}$), $L_{\text{TIR}} \propto \psi$, and the original form of the Kennicutt-Schmidt law ($\Sigma_{\text{SFR}} \propto \Sigma_{\text{gas}}^{1.4}$, Kennicutt 1998), the basic equation of $L_{\text{TIR}} \propto M_{\text{dIR}} T_d^{4+\beta}$ can be reduced to $\Sigma_{\text{TIR}} \propto T_d^{3.5(4+\beta)}$, which is close to the observed δ value with the emissivity index of $\beta \sim 1-2$.

Our result of $U_{\text{TIR}} \propto U_h \propto T_d^{4+\beta}$ for normal galaxies ($U_{\text{TIR}} \lesssim 30$) is equivalent to $\delta = 4 + \beta$, while the constant U_h for the circumnuclear starbursts ($U_{\text{TIR}} \gtrsim 30$) corresponds to $\delta = \infty$. The δ value obtained by C07 may be a result of the fit including the transition region of U_{TIR} between the two regimes. Their interpretation based on the Kennicutt-Schmidt law is not supported from our study, because we have seen that SFR is not proportional to L_{TIR} , and Σ_{dIR} is roughly constant against change of Σ_{gas} , for normal star-forming galaxies. There is a large scatter in the Kennicutt-Schmidt law, and it is unlikely that the tight correlation between U_h and U_{TIR} emerges from this law.

Besides the larger statistics, the strength of our study is that we estimated the dust-heating radiation field strength by fitting realistic physical dust models to the four AKARI/FIS photometric bands at 65–160 μm covering the broad thermal SED peak. It is good to use U_h instead of T_d to examine the correlation against U_{TIR} , because they have the same physical dimensions and hence not only the scaling between the two but also the ratio U_h/U_{TIR} is physically meaningful. It should also be noted that T_d is meaningful only for large grains in thermal equilibrium. Another important source of difference is that, as mentioned in §5.2, the AKARI-based samples include galaxies with smaller U_h than the IRAS-based samples used in the previous studies, which enabled us to clearly find the linear correlation between U_h and U_{TIR} in the normal galaxy regime.

7. Summary and Conclusions

We have constructed two new low-redshift galaxy samples based on the AKARI/FIS All Sky Bright Source Catalog: the AKARI-SDSS sample (878 galaxies) cross-correlated with the SDSS galaxies and available HI data, and the AKARI-HIPASS sample (711 galaxies) cross-correlated with the HIPASS HI galaxy catalog. To complement these for wider dynamic range of surface SFR density, the AKARI-SB sample (24 galaxies) has also been constructed from nearby circumnuclear starbursts. These samples include only galaxies having high quality AKARI/FIS fluxes at least in two bands to ensure the reliability of SED fittings.

We then studied these samples to understand the physics determining galactic-scale infrared SEDs, especially the broad thermal peak by large grains. The strength of dust-heating radiation field (U_h , roughly corresponding to the dust temperature as $U_h \propto T_d^{5.75}$), heated

dust mass (M_{dIR}), and total infrared luminosity (L_{TIR}) were derived from the fittings of physical dust models to the observed infrared SEDs, and their correlations with various physical quantities [optical size and luminosity, SFR (ψ), stellar mass (M_*), metallicity, and H I or H₂ gas masses] were investigated.

We found a tight power-law correlation between the L_{TIR}/ψ ratio and the specific SFR (SSFR, $\psi_s \equiv \psi/M_*$), as $L_{\text{TIR}}/\psi \propto \psi_s^{-0.54}$, which is valid except for very dusty galaxies having a large infrared-to-optical luminosity ratio (§5.1). Therefore SSFR is a good measure of the contribution from young stars to L_{TIR} . This relation may be useful to estimate the third parameter when two of SFR, M_* , and L_{TIR} are known. The widely used value of L_{TIR}/ψ as a SFR indicator is valid only for galaxies having largest SSFR of $\psi_s \gtrsim 0.1 \text{ Gyr}^{-1}$, and relatively aged stellar population must be taken into account in the dust-heating energy budget for most of the AKARI-SDSS galaxies.

The most important result of this work is the discovery of the tight linear correlation between U_h and galactic-scale mean infrared radiation field $U_{\text{TIR}} \propto L_{\text{TIR}}/(\pi R^2)$ for the AKARI-SDSS and AKARI-HIPASS samples, taking the r -band optical size as R (§5.3). The ratio of U_h/U_{TIR} is close to unity in the same physical units, and the physical dispersion along this relation in U_h is about 0.3 dex ($\sim 13\%$ in the dust temperature). This $U_{\text{TIR}}-U_h$ relation is nicely explained by a thin disk of dust-heating sources embedded in a thicker, optically-thick ($\tau_{d,\text{eff}}^{\text{tot}} \gtrsim 1$) dust disk (the case B2 in Fig. 15), where $\tau_{d,\text{eff}}^{\text{tot}}$ is the effective dust opacity averaged over wavelength with the weight of the SED of the interstellar radiation field (ISRF). This also means that infrared SEDs of galaxies are determined mainly by ISRF on a galactic scale, rather than those on smaller scales like individual star forming regions or molecular clouds.

The $U_{\text{TIR}}-U_h$ relation is particularly useful in theoretical modeling of infrared emission, giving a simple method to determine dust SED from L_{TIR} and R that can be predicted relatively easily in cosmological galaxy formation models. It may also be useful in observational studies; e.g., when flux of dust emission is available only in one band for a galaxy but its size is known, one can make a guess about the SED shape and L_{TIR} by searching for U_h that satisfies the relation of $U_{\text{TIR}} \sim U_h$.

Since only dust in the layer of one optical depth is heated, the dust column density estimated by infrared emission should be constant at $\Sigma_{\text{dIR}} \sim \Sigma_{d,\text{crit}}$ corresponding to $\tau_{d,\text{eff}} = 1$, which was also confirmed by our data. This interpretation predicts that the heated fraction of the total dust mass (M_{dIR}/M_d) scales with the total dust column density as $\propto \Sigma_d^{-1}$, and the observed trends of $M_{\text{dIR}}/M_{Z(\text{HI})} \propto \Sigma_{Z(\text{HI})}^{-1}$ and $M_{\text{dIR}}/M_{\text{HI}} \propto \Sigma_{\text{HI}}^{-1}$ support this expectation, where $Z(\text{HI})$ denotes the metal in H I gas phase (§5.4). An important implication is that, for many normal galaxies, the dust mass derived from infrared emission gives only a lower bound, with a significant amount of cold dust not contributing to infrared emission.

On the other hand, the data of the AKARI-SB sam-

ple indicate that there is an upper limit of $U_h \lesssim 50$ (in units of the local ISRF around the solar neighbourhood), and U_h becomes constant at this value for intensive starbursts having $U_{\text{TIR}} \gtrsim 50$ (§5.5). The H_2 mass is tightly correlated with the heated dust mass M_{dIR} , and the upper limit of U_h corresponds to the maximum star formation efficiency (SFE, defined as SFR per hydrogen gas mass) of $\psi_{e,\text{max}} \sim 10 \text{ Gyr}^{-1}$. This maximum SFE likely originates from the physics of star formation in ISM, and the spatial distribution of heating sources and dust changes from the case B2 to B1 (the same mixed distribution for stars and dust) in Fig. 15 around $U_{\text{TIR}} \sim 50$.

All the galaxies studied here seem optically thick to dust heating radiation. The distribution of $\tau_{d,\text{eff}}^{\text{tot}}$ extends down to $\tau_{d,\text{eff}}^{\text{tot}} \sim 1$, but there is a sharp drop of the number of optically thin galaxies at $\tau_{d,\text{eff}}^{\text{tot}} \lesssim 1$. We argued in §6.1 that this is unlikely to be a result of selection effects, but there seems a feedback effect to suppress the formation of optically thin galaxies. Because it is related to dust opacity, the feedback is likely by the photoelectric heating of ISM by dust grains. This process is known to be the major heating in many phases of ISM, and the self-shielding of dust-heating radiation on a galactic scale may be a necessary condition to avoid a global suppression of star formation. It is often stated that starburst galaxies are dusty, but if this hypothesis is true, one may rather state that they are starbursts *because* they are dusty.

We discussed implications of our results for galaxy formation in general. The strong dependence of galactic-scale gas cooling on $\tau_{d,\text{eff}}^{\text{tot}}$ may be responsible for the known correlation between HI mass and size ($M_{\text{HI}} \propto R^2$), which is on the line corresponding to $\tau_{d,\text{eff}}^{\text{tot}} \sim 1$ (§6.1). The Kennicutt-Schmidt law (SFR surface density Σ_{SFR} versus hydrogen gas surface density Σ_{H}) may be understood by the maximum SFE $\psi_{e,\text{max}}$ as the baseline with the strong dependence of SFE on $\tau_{d,\text{eff}}^{\text{tot}}$ by the feedback (§6.2). The feedback by dust opacity may also have interesting implications for galaxy formation in the cosmological context, because it would accelerate star formation in massive objects at high redshifts. Such an effect may be helpful to solve some of the problems currently discussed in the field of cosmological galaxy formation (§6.3).

It is quite intriguing to examine whether the scaling relations found in this work, especially $U_{\text{TIR}}-U_h$, hold also for high redshift galaxies. Planned infrared/submillimeter facilities will give such opportunities in the near future. Especially, ALMA will be a quite powerful facility for this purpose by the unprecedented flux sensitivity and angular resolution at wavelengths covering the thermal SED peak at high redshifts.

The electronic catalog data of the samples constructed in this work are available on request to the authors.

We would like to thank Y. Inoue for useful discussions. This work is based on observations with AKARI, a JAXA project with the participation of ESA. This work was supported in part by the Grant-in-Aid for Scientific Research (19740099 for TT, 20740105 and 23340046 for TTT,

22740123 for MN, and 22111506 for all) from the Ministry of Education, Culture, Sports, Science and Technology (MEXT). TT and RM were supported by the Global COE Program ‘‘The Next Generation of Physics, Spun from Universality and Emergence’’ from MEXT. TTT was supported by the Global COE Program ‘‘Quest for Fundamental Principles in the Universe: from Particles to the Solar System and the Cosmos’’ from MEXT. TTT was also supported by the Program for Improvement of Research Environment for Young Researchers from the Special Coordination Funds for Promoting Science and Technology. MARK was supported by the Research Fellowship for Young Scientists from the Japan Society for the Promotion of Science (JSPS).

References

- Bakes, E. L. O., & Tielens, A. G. G. M. 1994, ApJ, 427, 822
 Baugh, C. M., Lacey, C. G., Frenk, C. S., Granato, G. L., Silva, L., Bressan, A., Benson, A. J., & Cole, S. 2005, MNRAS, 356, 1191
 Baugh, C. M. 2006, Reports on Progress in Physics, 69, 3101
 Bell, E. F., et al. 2004, ApJ, 608, 752
 Benson, A. J., Bower, R. G., Frenk, C. S., Lacey, C. G., Baugh, C. M., & Cole, S. 2003, ApJ, 599, 38
 Bigiel, F., Leroy, A., Walter, F., Brinks, E., de Blok, W. J. G., Madore, B., & Thornley, M. D. 2008, AJ, 136, 2846
 Bigiel, F., Leroy, A., Walter, F., Blitz, L., Brinks, E., de Blok, W. J. G., & Madore, B. 2010, AJ, 140, 1194
 Binney, J. & Merrifield, M. 1998, Galactic Astronomy, Princeton Univ. Press (§9.2)
 Blanton, M. R., et al. 2005, AJ, 129, 2562
 Bohlin, R. C., Savage, B. D., & Drake, J. F. 1978, ApJ, 224, 132
 Boissier, S., Boselli, A., Buat, V., Donas, J., & Milliard, B. 2004, A&A, 424, 465
 Boquien, M., et al. 2010, ApJ, 713, 626
 Brinchmann, J., Charlot, S., White, S. D. M., Tremonti, C., Kauffmann, G., Heckman, T., & Brinkmann, J. 2004, MNRAS, 351, 1151
 Buat, V., Giovannoli, E., Takeuchi, T. T., Heinis, S., Yuan, F.-T., Burgarella, D., Noll, S., & Iglesias-Páramo, J. 2011, A&A, 529, A22
 Catinella, B., et al. 2010, MNRAS, 403, 683
 Chanical, P., Flores, H., Guiderdoni, B., Elbaz, D., Hammer, F., & Vigroux, L. 2007, A&A, 462, 81 (C07)
 Chapin, E. L., Hughes, D. H., & Aretxaga, I. 2009, MNRAS, 393, 653
 Chapman, S. C., Helou, G., Lewis, G. F., & Dale, D. A. 2003, ApJ, 588, 186
 Chary, R., & Elbaz, D. 2001, ApJ, 556, 562
 Cimatti, A., et al. 2004, Nature, 430, 184
 da Cunha, E., Charlot, S., & Elbaz, D. 2008, MNRAS, 388, 1595
 da Cunha, E., Eminian, C., Charlot, S., & Blaizot, J. 2010, MNRAS, 403, 1894
 Dale, D. A., Helou, G., Contursi, A., Silbermann, N. A., & Kolhatkar, S. 2001, ApJ, 549, 215
 Dale, D. A., & Helou, G. 2002, ApJ, 576, 159 (DH02)
 Desert, F.-X., Boulanger, F., & Puget, J. L. 1990, A&A, 237, 215
 Devereux, N. 1987, ApJ, 323, 91
 Dopita, M. A., et al. 2005, ApJ, 619, 755

- Doyle, M. T., et al. 2005, *MNRAS*, 361, 34
- Draine, B. T. 2003, *ARA&A*, 41, 241
- Draine, B. T., & Li, A. 2007, *ApJ*, 657, 810 (DL07)
- Draine, B. T., et al. 2007, *ApJ*, 663, 866
- Dunne, L., Eales, S., Edmunds, M., Ivison, R., Alexander, P., & Clements, D. L. 2000, *MNRAS*, 315, 115
- Dunne, L., Eales, S. A., & Edmunds, M. G. 2003, *MNRAS*, 341, 589
- Evans, N. J., et al. 2009, *ApJS*, 181, 321
- Fisher, K. B., Huchra, J. P., Strauss, M. A., Davis, M., Yahil, A., & Schlegel, D. 1995, *ApJS*, 100, 69
- Fontanot, F., Monaco, P., Silva, L., & Grazian, A. 2007, *MNRAS*, 382, 903
- Fuchs, B., Jahreiß, H., & Flynn, C. 2009, *AJ*, 137, 266
- Galliano, F., Madden, S. C., Jones, A. P., Wilson, C. D., Bernard, J.-P., & Le Peintre, F. 2003, *A&A*, 407, 159
- Galliano, F., Madden, S. C., Jones, A. P., Wilson, C. D., & Bernard, J.-P. 2005, *A&A*, 434, 867
- Gao, Y., & Solomon, P. M. 2004, *ApJ*, 606, 271
- Garcia-Appadoo, D. A., West, A. A., Dalcanton, J. J., Cortese, L., & Disney, M. J. 2009, *MNRAS*, 394, 340
- Giovanelli, R., et al. 2007, *AJ*, 133, 2569
- Glazebrook, K., et al. 2004, *Nature*, 430, 181
- Goto, T., et al. 2011a, *MNRAS*, 410, 573
- Goto, T., et al. 2011b, *MNRAS*, 414, 1903
- Granato, G. L., Lacey, C. G., Silva, L., Bressan, A., Baugh, C. M., Cole, S., & Frenk, C. S. 2000, *ApJ*, 542, 710
- Grevesse, N., Asplund, M., Sauval, A. J., & Scott, P. 2010, *Ap&SS*, 328, 179
- Guideroni, B., Hivon, E., Bouchet, F. R., & Maffei, B. 1998, *MNRAS*, 295, 877
- Hauser, M. G., & Dwek, E. 2001, *ARA&A*, 39, 249
- Haynes, M. P., & Giovanelli, R. 1984, *AJ*, 89, 758
- Heithausen, A., & Mebold, U. 1989, *A&A*, 214, 347
- Hildebrand, R. H. 1983, *QJRAS*, 24, 267
- Hunt, L., Bianchi, S., & Maiolino, R. 2005, *A&A*, 434, 849
- Hwang, H. S., et al. 2010, *MNRAS*, 409, 75
- Ishihara, D., et al. 2010, *A&A*, 514, A1
- Issa, M. R., MacLaren, I., & Wolfendale, A. W. 1990, *A&A*, 236, 237
- James, A., Dunne, L., Eales, S., & Edmunds, M. G. 2002, *MNRAS*, 335, 753
- Kauffmann, G., et al. 2003, *MNRAS*, 341, 33
- Kawada, M., et al. 2007, *PASJ*, 59, 389
- Kennicutt, R. C., Jr. 1998, *ApJ*, 498, 541 (K98)
- Kent, B. R., et al. 2008, *AJ*, 136, 713
- Kovács, A., Chapman, S. C., Dowell, C. D., Blain, A. W., Ivison, R. J., Smail, I., & Phillips, T. G. 2006, *ApJ*, 650, 592
- Kroupa, P. 2001, *MNRAS*, 322, 231
- Lagache, G., Dole, H., & Puget, J.-L. 2003, *MNRAS*, 338, 555
- Lehnert, M. D., & Heckman, T. M. 1996, *ApJ*, 472, 546 (LH96)
- Li, A., & Draine, B. T. 2001, *ApJ*, 554, 778
- Małek, K., Pollo, A., Takeuchi, T. T., Bienias, P., Shirahata, M., Matsuura, S., & Kawada, M. 2010, *A&A*, 514, A11
- Malhotra, S. 1994, *ApJ*, 433, 687
- Malhotra, S. 1995, *ApJ*, 448, 138
- Mathis, J. S., Mezger, P. G., & Panagia, N. 1983, *A&A*, 128, 212
- Meyer, M. J., et al. 2004, *MNRAS*, 350, 1195
- Moustakas, J., Kennicutt, R. C., Jr., Tremonti, C. A., Dale, D. A., Smith, J.-D. T., & Calzetti, D. 2010, *ApJS*, 190, 233
- Muñoz-Mateos, J. C., et al. 2009, *ApJ*, 701, 1965
- Murakami, H., et al. 2007, *PASJ*, 59, 369
- Nair, P. B., van den Bergh, S., & Abraham, R. G. 2010, *ApJ*, 715, 606
- Onaka, T., et al. 2007, *PASJ*, 59, 401
- Phillipps, S., & Disney, M. 1988, *MNRAS*, 231, 359
- Press, W.H., Teukolsky, S.A., Vetterling, W.T., & Brian P. Flannery, B.P. 2007, *Numerical Recipes 3rd Edition: The Art of Scientific Computing* (Cambridge Univ. Press)
- Rachford, B. L., et al. 2009, *ApJS*, 180, 125
- Rosenberg, J. L., & Schneider, S. E. 2003, *ApJ*, 585, 256
- Rubin, D., et al. 2009, *A&A*, 494, 647
- Rujopakarn, W., Rieke, G. H., Eisenstein, D. J., & Juneau, S. 2011a, *ApJ*, 726, 93
- Rujopakarn, W., Rieke, G. H., Weiner, B. J., et al. 2011b, arXiv:1107.2921
- Salim, S., et al. 2007, *ApJS*, 173, 267
- Salim, S., et al. 2009, *ApJ*, 700, 161
- Salpeter, E. E. 1955, *ApJ*, 121, 161
- Schmidt, M. 1959, *ApJ*, 129, 243
- Silk, J. 2011, arXiv:1102.0283
- Silva, L., Granato, G. L., Bressan, A., & Danese, L. 1998, *ApJ*, 509, 103
- Soifer, B. T., Sanders, D. B., Madore, B. F., Neugebauer, G., Danielson, G. E., Elias, J. H., Lonsdale, C. J., & Rice, W. L. 1987a, *ApJ*, 320, 238
- Soifer, B. T., Neugebauer, G., & Houck, J. R. 1987b, *ARA&A*, 25, 187
- Soifer, B. T., & Neugebauer, G. 1991, *AJ*, 101, 354
- Springob, C. M., Haynes, M. P., Giovanelli, R., & Kent, B. R. 2005, *ApJS*, 160, 149
- Stierwalt, S., Haynes, M. P., Giovanelli, R., Kent, B. R., Martin, A. M., Saintonge, A., Karachentsev, I. D., & Karachentseva, V. E. 2009, *AJ*, 138, 338
- Strateva, I., et al. 2001, *AJ*, 122, 1861
- Sun, A.-L., & Hirashita, H. 2011, *MNRAS*, 411, 1707
- Takagi, T., Vansevicius, V., & Arimoto, N. 2003a, *PASJ*, 55, 385
- Takagi, T., Arimoto, N., & Hanami, H. 2003b, *MNRAS*, 340, 813
- Takeuchi, T. T., Ishii, T. T., Hirashita, H., Yoshikawa, K., Matsuhara, H., Kawara, K., & Okuda, H. 2001, *PASJ*, 53, 37
- Takeuchi, T. T., Buat, V., & Burgarella, D. 2005, *A&A*, 440, L17
- Takeuchi, T. T., Buat, V., Heinis, S., Giovannoli, E., Yuan, F.-T., Iglesias-Páramo, J., Murata, K. L., & Burgarella, D. 2010, *A&A*, 514, A4
- Tojeiro, R., Wilkins, S., Heavens, A. F., Panter, B., & Jimenez, R. 2009, *ApJS*, 185, 1
- Totani, T., & Takeuchi, T. T. 2002, *ApJ*, 570, 470
- Tremonti, C. A., et al. 2004, *ApJ*, 613, 898
- Valiante, E., Lutz, D., Sturm, E., Genzel, R., & Chapin, E. L. 2009, *ApJ*, 701, 1814
- van der Kruit, P. C., & Freeman, K. C. 2011, arXiv:1101.1771
- Vladimir, G., Centurión, M., Levshakov, S. A., Péroux, C., Khare, P., Kulkarni, V. P., & York, D. G. 2006, *A&A*, 454, 151
- Walcher, J., Groves, B., Budavári, T., & Dale, D. 2011, *Ap&SS*, 331, 1
- Walterbos, R. A. M., & Greenawalt, B. 1996, *ApJ*, 460, 696
- Weingartner, J. C., & Draine, B. T. 2001, *ApJ*, 548, 296
- West, A. A., Garcia-Appadoo, D. A., Dalcanton, J. J., Disney, M. J., Rockosi, C. M., Ivezić, Ž., Bentz, M. C., & Brinkmann, J. 2010, *AJ*, 139, 315

- Wolfire, M. G., Hollenbach, D., McKee, C. F., Tielens, A. G. G. M., & Bakes, E. L. O. 1995, *ApJ*, 443, 152
- Wu, J., Evans, N. J., II, Gao, Y., Solomon, P. M., Shirley, Y. L., & Vanden Bout, P. A. 2005, *ApJL*, 635, L173
- Yamamura, I., et al. 2010, AKARI-FIS Bright Source Catalogue Release Note Version 1.0
- Yuan, F.-T., Takeuchi, T. T., Buat, V., Heinis, S., Giovannoli, E., Murata, K. L., Iglesias-Páramo, J., & Burgarella, D. 2011, to appear in *PASJ*